Hybrid Photonic Crystal Nanobeam Cavities: Design, Fabrication and Analysis

by

Ishita Mukherjee
Bachelor of Technology, West Bengal University of Technology, 2010

A Thesis Submitted in Partial Fulfillment
of the Requirements for the Degree of

MASTER OF APPLIED SCIENCE

in the Department of Electrical and Computer Engineering

Supervisory Committee

Hybrid Photonic Crystal Nanobeam Cavities: Design, Fabrication and Analysis

by

Ishita Mukherjee
Bachelor of Technology, West Bengal University of Technology, 2010

Supervisory Committee

Dr. Reuven Gordon, Department of Electrical and Computer Engineering
Supervisor

Dr. Harry H.L. Kwok, Department of Electrical and Computer Engineering
Departmental Member

Dr. Martin B.G. Jun, Department of Mechanical Engineering
Outside Member

Abstract

Supervisory Committee
Dr. Reuven Gordon, Department of Electrical and Computer Engineering
Supervisor

Dr. Harry H. L. Kwok, Department of Electrical and Computer Engineering
Departmental Member

Dr. Martin B.G. Jun, Department of Mechanical Engineering
Outside Member

Photonic cavities are able to confine light to a volume of the order of wavelength of light and this ability can be described in terms of the cavity's quality factor, which in turn, is proportional to the confinement time in units of optical period. This property of the photonic cavities have been found to be very useful in cavity quantum electrodynamics, for e.g., controlling emission from strongly coupled single photon sources like quantum dots. The smallest possible mode volume attainable by a dielectric cavity, however, poses a limit to the degree of coupling and therefore to the Purcell effect. As metal nanoparticles with plasmonic properties can have mode volumes far below the diffraction limit of light, these can be used to achieve stronger coupling, but the lossy nature of the metals can result in extremely poor quality factors. Hence a hybrid approach, where a high-quality dielectric cavity is combined with a low-quality metal nanoparticle, is being actively pursued. Such structures have been shown to have the potential to preserve the best of both worlds.

This thesis describes the design, fabrication and characterization of hybrid plasmonic – photonic nanobeam cavities. Experimentally, we were able to achieve a quality factor of 1200 with the hybrid approach, which suggests that the results are promising for future single photon emission studies. It was found that modeling the behaviour (resonant frequencies, quality factors) of these hybrid cavities with conventional computation methods like FDTD can be tedious, for e.g., a comprehensive study of the electromagnetic fields inside a hybrid photonic nanobeam cavity has been found to take

up to 48 hours with FDTD. Hence, we also present an alternate method of analysis using perturbation theory, showing good agreement with FDTD.

Table of Contents

SUPERVISORY COMMITTEE ..... **II**
ABSTRACT ..... **III**
TABLE OF CONTENTS ..... **V**
LIST OF FIGURES ..... **VII**
ACKNOWLEDGMENTS ..... **XI**
DEDICATION ..... **XII**
GLOSSARY ..... **XIII**
1. THESIS INTRODUCTION **1**
1.1. THESIS ORGANIZATION 2
2. LITERATURE REVIEW **3**
2.1. INTRODUCTION 3
2.2. OPTICAL MICROCAVITIES 3
2.2.1. Fabry-Perot Micropost Cavities *4*
2.2.2. Whispering Gallery Mode Cavities *5*
2.2.3. Photonic Crystal Cavities *6*
2.3. PURCELL EFFECT 9
2.4. SURFACE PLASMONS 10
2.4.1 Localized Surface Plasmons *12*
2.4.2 Mode Volume of Plasmonic Cavities *13*
2.4.3 Losses in Metals *15*
2.5. PLASMONIC-PHOTONIC HYBRID CAVITIES 17
2.5.1. Application to Single Photon Sources *19*
2.6. THEORETICAL MODELING OF HYBRID CAVITIES 21
2.6.1. Perturbation Theory *22*
2.7. SUMMARY 25
3. NANOFABRICATION, MEASUREMENT AND DESIGN TECHNIQUES **26**
3.1. INTRODUCTION 26
3.2. SCANNING ELECTRON MICROSCOPY 26
3.2.1. Working Principle *27*
3.2.2. Imaging Instabilities *28*
3.2.3. Energy Dispersive X-ray Spectroscopy *30*
3.3. FOCUSSED ION BEAM MILLING 31
3.3.1. Working Principle *31*
3.3.2. Fabrication Concerns *32*
3.4. FLUORESCENCE MICROSCOPY 33
3.5. FINITE DIFFERENCE TIME DOMAIN (FDTD) MODELLING 34
3.5.1. Computational Domain & Materials *35*
3.5.2. Sources *38*

3.6. SUMMARY 39

4. INTEGRATION OF METAL NANOPARTICLE IN PHOTONIC CRYSTAL NANOBEAM CAVITY 40

4.1. INTRODUCTION 40
4.2. DESIGN OF THE HYBRID PHOTONIC CRYSTAL NANOBEAM / SILVER NANOPARTICLE STRUCTURE 40
4.2.1. Quality Factor Calculation 41
4.3. NANOPARTICLE SYNTHESIS 43
4.4. FABRICATION PROCEDURE 44
4.5. EDX MEASUREMENTS 46
4.6. IMAGING NANOBEAM CAVITIES WITH SEM 47
4.7. FLUORESCENCE MEASUREMENTS 48
4.7.1. Measurement Results 49
4.8. MEASUREMENTS ON A SINGLE CAVITY WITH AND WITHOUT THE AG NANOPARTICLE 52
4.9. DISCUSSION 52
4.10. SUMMARY 53

5. ANALYSIS OF HYBRID PLASMONIC-PHOTONIC CRYSTAL STRUCTURES USING PERTURBATION THEORY 54

5.1. INTRODUCTION 54
5.2. PERTURBATION THEORY APPLICATION TO A HYBRID PLASMONIC-PHOTONIC STRUCTURE 54
5.2.1. Introduction of Scattering Losses 54
5.2.2. Applying Perturbation Theory to a Nanobeam Cavity with Ag Nanoparticle 55
5.3. THEORY RESULTS AND VERIFICATION 57
5.3.1. Calculation with a Photonic Nanobeam Cavity 57
5.3.2. Calculation with a Waveguide Cavity 59
5.3.3. Discussion 59
5.4. FDTD SOLVERS ON SUPERCOMPUTER CLUSTERS 60
5.5. SUMMARY 60

6. CONCLUSION AND FUTURE WORK 62

6.1. FUTURE WORK 63

BIBLIOGRAPHY 64

APPENDIX A 68

MATLAB CODE FOR LORENTZIAN FITTING 68

APPENDIX B 70

MATLAB CODE FOR APPLYING PERTURBATION FORMULA ON SIMULATION DATA 70

List of Figures

Figure 2.1 Different types of optical microcavities. (Reprinted by permission from MacMillan Publishers Ltd.: Nature ©2003) [16]. 4

Figure 2.2 (a) A typical PL spectrum of measurement showing a cavity resonance mode at ~930 nm and a Scanning Electron Microscope (SEM) image of a micropost optical cavity [17]. ©1998 American Physical Society. (b) A schematic showing a single photon source (quantum dot) at the center of the cavity [16]. 5

Figure 2.3 (a) A representation of Whispering Gallery mode (b) An SEM image of a fabricated silica micro disc (c) A ringdown measurement of the microcavity yields a critical lifetime of 43 ns which corresponds to a Q factor of 1.25×10^8 (Reprinted by permission from MacMillan Publishers Ltd.: Nature ©2003) [18]. 6

Figure 2.4 A schematic representation of a plane wave travelling through a photonic crystal. denotes the wave vector of the travelling wave. 7

Figure 2.5 (a) H1 type photonic crystal cavity on GaAs substrate with an experimentally measured Q factor of ~3000 at a wavelength of ~995 nm [20]. (b) L3 type photonic crystal cavity on Silicon Nitride (Si_3N_4) substrate with resonant mode in the visible range. Q=1460 at ~660 [21]. (c) Double heterstrocture waveguide cavity on Si_3N_4 with Q=3411 at ~668.5 nm. Reprinted with permission from [22] ©2008 American Institute of Physics. 8

Figure 2.6 (a) A nanobeam photonic cavity fabricated on Silicon Nitride. (b) Fluorescence measurement performed on the cavity show a quality factor of ~55,000 at ~624 nm [23]. 9

Figure 2.7 (a) Interface between two media (1 and 2) with separate dielectric functions [26]. (b) Dispersion curve of surface plasmons lies to the right of light line showing $k_{spp} > k$ 12

Figure 2.8 (a) Different shapes of gold nanoparticles produce different resonance spectra [28] (Reprinted with permission). (b) The Lycurgus glass cup, demonstrating the bright red color of gold nanocrystals in transmitted light (c) SEM image of a typical nanocrystal embedded in the glass (Courtesy: British museum). ©2005 American Institute of Physics 13

Figure 2.9 (a) The mode length of 1D plasmonic cavities can be made smaller than the diffraction limit of light by decreasing the cavity width. (b) Ratio of cavity quality to mode volume for a 3D plasmonic cavity increases exponetially with decreasing cavity width [29] (©2006 IEEE). 14

Figure 2.10 (a) Metal nanoparticles placed in the path of an incident beam absorb and scatter light, so that power of the beam received by detector D is less than the power of the incident beam. (b) A single metal particle in a non absorbing medium illuminated by a plane wave [31]. 16

Figure 2.11 (a) SEM image of a fabricated silver-coated Surface Plasmon Polariton (SPP) microdisk resonator (left) and cavity mode dispersion curves for the resonator (right)

showing the mode confinement hotspots (Reprinted by permission from MacMillan Publishers Ltd.: Nature ©2009) [33]. (b) SEM image of a photonic cavity with plasmonic nanoantenna at the center (left) and electric field profile of the cavity with the nanoantenna at showing strongly damped cavity resonance mode (right). Reprinted with permission from [34] ©2008 American Chemical Society. 17

Figure 2.12 (a) Placement technique of gold nanoparticles in a double heterostructure photonic cavity using AFM tip. (b) AFM images of the cavity with a gold nanorod placed at the center in different orientations. (c) Resonance peaks of the two resonant modes of the cavity (top), resonance peaks for the configuration shown in 2.12b-left (middle) and reosnance peaks for 2.12b-right (bottom). Red and blue curves refer to excitation polarizations perpendicular and parallel to the waveguide axis, respectively. Reprinted with permission from [35] ©2010 American Chemical Society. 18

Figure 2.13 (a) A 3D schematic view of a single photon source containing a cavity region embedded between a 32-period bottom AlGaAs/GaAs DBR and a 23-period top DBR (white/blue layers). The cavity contains a single layer of InAs QDs (grey) and a mode-confining tapered AlOx region (dark blue). (b) Microcavities with various trench designs to control emission from embedded quantum dot emitters. Reprinted by permission from MacMillan Publishers Ltd.: Nature Photonics ©2007 [13]. 20

Figure 2.14 (a) SEM image of fabricated five-element Yagi-Uda antenna consisting of a feed element, one reflector, and three directors. A QD is attached to one end of the feed element (marked in red). (b) Comparison of SEM and scanning confocal luminescence microscopy images of three antennas driven by QDs. (c) Intensity time trace of luminescence in two different polarizations for one of the antennas in 2.14b, showing blinking of a single QD [39] (Reprinted with permission from AAAS). 21

Figure 2.15 Electric field distribution in the neighbourhood of a dielectric sphere, the field being uniform and equal to E1 in the absence of the sphere. 25

Figure 3.1 (a) Hitachi S-4800 SEM at the Advanced Microscopy Facility at UVic (Courtesy: Uvic AM Facility website). (b) Different types of information about a sample that can be obtained from SEM. 27

Figure 3.2 Sample irradiation by electron beam inside SEM column. 28

Figure 3.3 (a) Distorted image due to charging (b) uneven image brightness (c) sample contamination 30

Figure 3.4 EDX pulse analyzer output detecting the presence of silver (Ag), silicon nitride (Si, N) and aluminum (Al- from the sample stage) in a given sample. 30

Figure 3.5 Hitachi FB-2100 FIB at Advanced Microscopy Facility at UVic (Courtesy: Uvic AM Facility website).....31

Figure 3.6 Sputtering (left) and deposition (right) with FIB 32

Figure 3.7 (a) Poor selection of beam caused insufficient material removal from the top of the fabricated structure. (b) Badly aligned beam damaged the shape of the holes. (c) Well aligned beam resulted in circular holes. 33

Figure 3.8 A fluorescence microscope setup 34

Figure 3.9 (a) Actual shape of the structure to be simulated. (b) Structure discretized with 5 nm size mesh. 36

Figure 3.10 Graded mesh uses finer mesh cells near the interfaces and larger mesh cells in the bulk region (right) which reduces memory and computation time requirements than uniform mesh (left).....37

Figure 3.11 Comparison between default fit of the FDTD model to the complex material data and an optimum fit that can be obtained by adjusting fit parameters 38

Figure 3.12 (a) A mode source injected at one end of a photonic nanobeam cavity inside a simulation region (outlined in orange). The direction of propagation is depicted by the pink arrow (b) An electric dipole located at an asymmetric region at the center of the nanobeam. The double sided blue arrow shows the direction of dipole polarization. 39

Figure 4.1 Schematic showing the arrangement of the hole radii and periodicities for a four-hole taper beam photonic cavity with the desired location of the metal nanoparticle. 41

Figure 4.2 (a) Decaying electric fields with time. (b) Cavity resonance peak predicted at 602.24 nm.....42

Figure 4.3 (a) Electric field distribution 5 nm above the nanobeam without the Ag nanoparticle at 602.24 nm (logscale). (b) Electric field distribution at the same height above the nanobeam with the Ag nanoparticle at 611.14 nm (logscale). 43

Figure 4.4 (a) Silver particle after 24 hours of irradiation showed on Si3N4 (b) silver prism after 72 hours of irradiation showed on gold (c) Extinction spectrum of aqueous suspension of silver nanoparticles synthesized in our lab, showing a peak at 610 nm. 44

Figure 4.5 (a) SEM image of a 9×9 Si_3N_4 TEM grid from Ted Pella Inc. used for all fabrications (b)SEM image of a FIB fabricated photonic crystal nanobeam cavity on Si_3N_4. (Inset) Photonic crystal nanobeam cavity showing an ellipsoid nanoparticle at the centre.....46

Figure 4.6 Photonic nanobeam cavity damaged by excessive carbon paste leakage underneath. 48

Figure 4.7 Schematic showing the fluorescence microscopy setup and the actual laser spot focused at the center of one of the characterized nanobeams.(Inset) Schematic of the laser spot focused off-center on the nanobeam. 49

Figure 4.8 (a) Fluorescence emission spectrum and (b) Lorentzian fit on cavities without nanoparticle (blue). (c) Fluorescence emission spectrum and (d) Lorentzian fit on cavities with nanoparticle (red). Data points are shown in black. (e) Linewidth and wavelength of the fabricated cavities without (blue) and with (red) the nanoparticle. (f) Net intensity counts (peak count-average background count) achieved from the cavities at various resonance wavelengths. 51

Figure 4.9 Measurements taken from the same cavity before (red) and after (blue) the removal of the nanoparticle. (Inset) Zoom in on the blue curve showing the decreased intensity counts and linewidth compared to the red. 52

Figure 5.1 (a) 3D schematic showing the photonic crystal nanobeam with a nanoparticle inside the simulation region. The pink arrow shows the direction of the propagation of the mode. The inset is a close-up on the nanoparticle at the center. (b) Top view of the nanobeam in the simulation region, forming an unperturbed cavity. (c) Zoom-in to the center of the nanobeam after the introduction of the nanoparticle. The shaded area shows the perturbed region considered. 56

Figure 5.2 (a) The scattering cross Section of a 60×52×10 nm^3 silver nanoparticle on a 200 nm thick blank Si_3N_4 substrate. (b) A transverse cross Section through the nanoparticle showing the electric field distribution inside (linear scale). 57

Figure 5.3 The shift in the photonic nanobeam cavity frequency and the change in the quality factor with and without (blue) the addition of the nanoparticle from FDTD simulations (black) and perturbation theory (red). 60

Acknowledgments

I would like to sincerely thank my supervisor Dr. Reuven Gordon for his support and guidance throughout my Masters.

I would also like to convey my appreciation for Dr. Jeff Young of UBC for his invaluable inputs from time to time and British Columbia Innovation Council for supporting my research.

A special thank you to Dr. Elaine Humphrey and Adam Schuetze for their valuable guidance throughout all nanofabrication processes.

Thanks to all my friends at University of Victoria for their insightful advice in technical matters and for being pillars of support in times of need.

Finally, without the relentless support of my parents, this endeavor would never have seen the daylight. Thanks to both of you.

Dedication

To my family

and

Madhuchhanda Dutta

(1988-2005)

Glossary

AFM	Atomic Force Microscope
BSPP	Bis Phenylphosphine dihydrate di-Potassium
CCD	Charge-Coupled Device
CQED	Cavity Quantum ElectroDynamics
DBR	Distributed Bragg Reflector
EBL	Electron Beam Lithography
EDS / EDX	Energy Dispersive X-Ray Spectroscopy
FDTD	Finite Difference Time Domain
FIB	Focussed Ion Beam
FWHM	Full Width Half Maximum
HPC	High Performance Computing
LMIS	Liquid Metal Ion Source
PEC	Perfect Electric Conductor
PML	Perfectly Matched Layer
QD	Quantum Dot
SEM	Scanning Electron Microscope
SNR	Signal to Noise ratio
SPS	Single Photon Source
SPP	Surface Plasmon Polariton
SSD	Solid State Detector
TEM	Transmission Electron Microscopy

1. Thesis Introduction

Nanotechnology is the engineering of functional systems at a molecular and atomic scale. At this level, material properties change significantly compared to their bulk counterpart, which, if harnessed properly, has the potential to revolutionize many aspects of current technology. Quantum dots, for example, are tiny light-producing cells that could be used for illumination or for purposes such as display screens. Silicon chips can already contain millions of components, but this technology is reaching its limit. At a certain point, circuits become so small, that if one molecule is out of place, the circuit is likely to fail. Nanotechnology, in this case, will allow circuits to be constructed very accurately, even on an atomic level.

Cavity quantum electrodynamics (CQED) is the study of the interaction between light confined in a reflective cavity and atoms or other particles, under conditions where the quantum nature of light photons is significant [1]. CQED experiments implement a simple situation whose results can be cast in terms of the fundamental postulates of quantum theory. A CQED based qubit, which is the quantum computing equivalent of a bit in a conventional computer, can therefore be built, in principle.

All qubits involve entanglement of two or more entities [2] and in the simplest CQED scheme, these entities are a quantum emitter (an atom that emits light with a very precise color, e.g. quantum dots) and the quantum of light it emits (a photon). The entanglement requires precise control over the interactions between electron excitation of the emitter and the light it emits. This control is achieved by building ultra-small cavities that trap photons of interest in the vicinity of the emitter while time-shielding the latter from other photons [3-5]. These optical dielectric cavities, although capable of producing high quality factors, are fundamentally limited to have characteristic sizes of the order of the wavelength of light [6, 7], whereas even large quantum emitters are more than a hundred times smaller than the lowest achievable size of the dielectric cavities. This makes the strength of coupling between the emitter and the quantum dots marginal at its best. Quantum emitters (e.g., single photon sources) on the other hand, are able to couple strongly with metal nanoparticles, due to plasmonic effects of the latter [8, 9], but losses associated with metals are detrimental to the quality factor [10, 11]. The aim, as a whole,

is to amplify the emission strength of the quantum emitter by strategically placing the emitter on a nanoparticle and coupling the latter to a low-loss dielectric cavity. This enhancement in emission is explained by Purcell effect which states that, the radiation properties of an atom can be changed by controlling the boundary conditions of the electromagnetic field with mirrors or cavities [12].

The research work described in this thesis addresses the above problem. It presents successful realization of dielectric photonic cavities, each strongly coupled to a single metal nanoparticle, and exhibiting Purcell effect. The photonic cavities have been fabricated using focussed ion beam (FIB) milling. Characterizations of the combined devices were carried out using fluorescence microscopy. Theoretical analyses of such devices were performed applying perturbation theory.

1.1. Thesis Organization

Chapter 2 provides a brief account of the general theory behind optical microcavities, their types and short comings. It also reviews the properties of surface plasmons and how these can be harnessed to create hybrid plasmonic-photonic devices. A concise derivation of perturbation theory is provided.

Chapter 3 provides short introduction to various nanofabrication, measurement and modeling techniques used in this research to achieve the results as well as talks about certain measures that can be taken to address fabrication and imaging concerns.

Chapter 4 describes in detail about the fabrication of photonic nanobeam cavities using FIB, their integration to single silver nanoparticles and experimental results obtained from fluorescence measurements of the cavities.

Chapter 5 elaborates how perturbation theory can be used in theoretical analysis of the hybrid cavities and the advantages it offers over comprehensive simulation techniques like Finite Difference Time Domain (FDTD).

Chapter 6 summarizes the work done and outlines its possible future directions.

2. Literature Review

2.1. Introduction

This Chapter provides a brief overview of different types of optical microcavities and how the properties of surface plasmons can be used to localize and enhance spontaneous emission from the cavities. It reviews the experimental works that have, so far, been done in order to achieve a compromise between the high quality factors of dielectric cavities and the strong local field enhancements offered by surface plasmons in metal nanoparticles. In addition, a modelling technique based on perturbation theory, in order to theoretically predict or verify the experimental results is presented.

2.2. Optical Microcavities

Optical microcavities are micro or nanoscale structures that are able to confine light to a volume of the order of the wavelength of light, by resonant recirculation. Because of this light confining property, optical microcavities can control the distribution of the radiated power and spectral width of the emitted light, which is useful in enabling long distance data transmission over optical fibers. Optical microcavities can also enhance or suppress spontaneous emission rates of photons, and control the directionality of emission, even for single photon sources [13, 14]. This property is particularly important in developing quantum encryption systems. In addition, they allow for ultra-efficient and compact laser sources with enhanced functionalities [15].

Depending on the characteristics of the structure and the nature of the material, the wavelength of light that forms a standing wave inside the structure, forms the resonant mode of the cavity. The extent of confinement of this resonant mode can be measured in terms of the cavity's quality factor or Q factor. An ideal cavity with no loss would confine light indefinitely and therefore possess a Q factor of infinity [16]. In real cases therefore, the goal is to realize microcavities that, while taking into account the dissipative mechanisms, would still possess a high Q factor.

There have been many attempts over the years to demonstrate high quality optical microcavities. Figure 2.1 shows the three most predominant types.

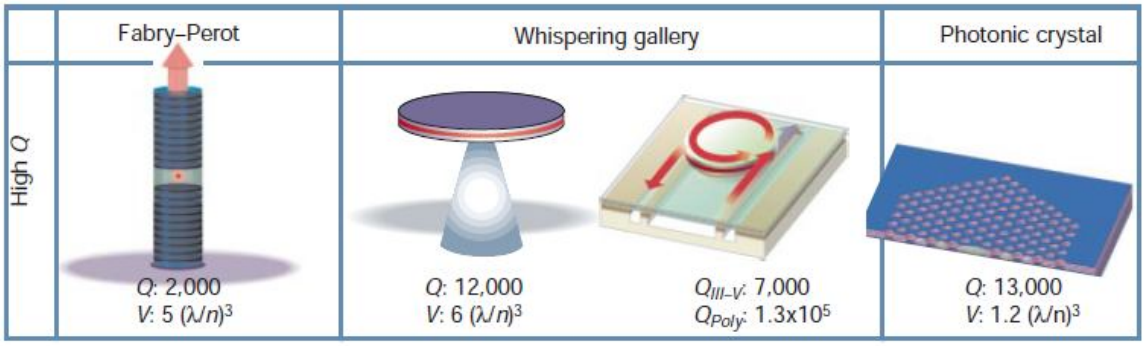

Figure 2.1 Different types of optical microcavities. (Reprinted by permission from MacMillan Publishers Ltd.: Nature ©2003) [16].

2.2.1. Fabry-Perot Micropost Cavities

A Fabry-Perot type resonance occurs when light bounces back and forth between two opposite reflective surfaces (mirrors) of a resonator of length L and due to the effects of interference, only certain frequencies of radiation are sustained. Each of these frequencies forms a resonance mode. The micropost cavity acts along the same principle. By selectively etching a GaAs/AlAs planar microcavity, it is possible to create stacked Distributed Bragg Reflectors (which will act as mirrors) of circular cross sections, inside the cavity [17]. The 15 period Bragg reflectors on the top and the 25 period Bragg reflectors in the bottom are separated by a plain layer of GaAs (see Figure 2.2). Such an arrangement, measured with photoluminescence spectroscopy, has been found to produce a Q factor of ~5000.

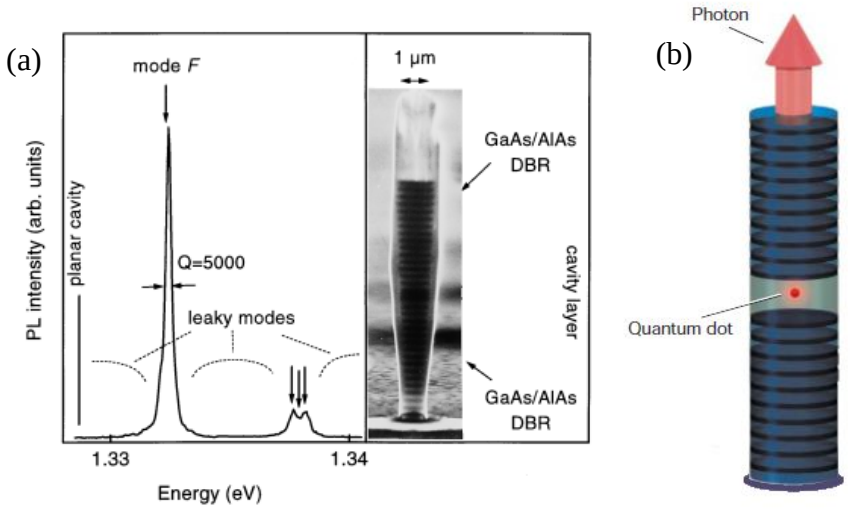

Figure 2.2 (a) A typical PL spectrum of measurement showing a cavity resonance mode at ~930 nm and a Scanning Electron Microscope (SEM) image of a micropost optical cavity [17]. ©1998 American Physical Society. (b) A schematic showing a single photon source (quantum dot) at the center of the cavity [16].

2.2.2. Whispering Gallery Mode Cavities

Named after the whispering gallery of St. Paul's cathedral in London, Whispering Gallery resonators are spherical or disc-shaped dielectric structures following the principle of continuous total internal reflection. As light travels around the edge of the sphere, it is totally internally reflected at every bounce and undergoes interference with itself. This allows only whole number of wavelengths to 'fit' along the edge of the sphere, which causes the creation of extremely low loss 'whispering gallery' modes in the cavity.

2 μm thick Silica discs manipulated photolithographically to the desired diameter and supported on circular silicon pillars, have been found to support a ultra-high Q factor in excess of 1×10^8(see Figure 2.3) [18]. The disc supports the modes of interest while the silicon pillar below prevents power leakage into the substrate.

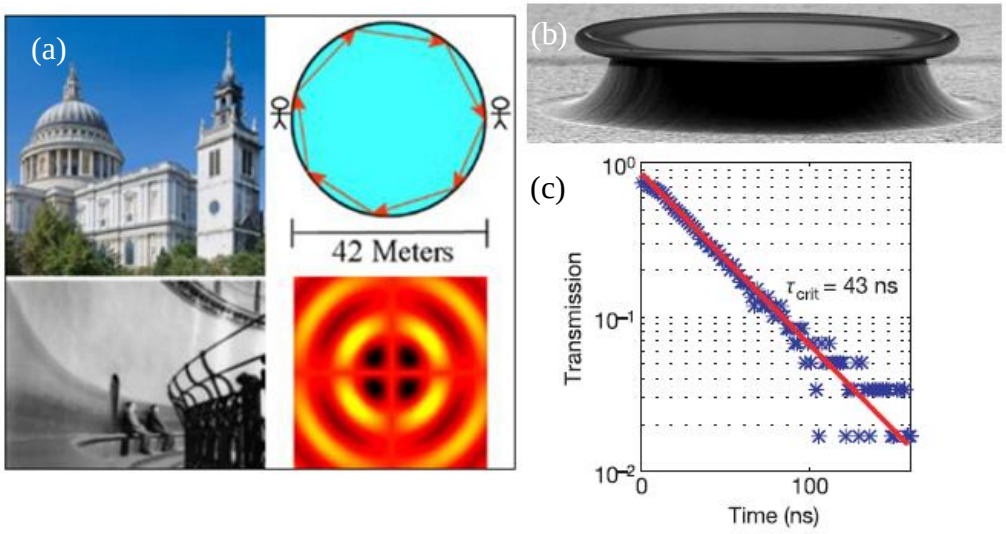

Figure 2.3 (a) A representation of Whispering Gallery mode (b) An SEM image of a fabricated silica micro disc (c) A ringdown measurement of the microcavity yields a critical lifetime of 43 ns which corresponds to a Q factor of 1.25×10^8 (Reprinted by permission from MacMillan Publishers Ltd.: Nature ©2003) [18].

2.2.3. Photonic Crystal Cavities

Photonic crystals are dielectric or metallo-dielectric nanostructures with spatially periodic dielectric constant. Because of the periodicity in between similar dielectric constant regions (see Figure 2.4), some wavelengths of light in the material ($\lambda\sim2a$) are not allowed to travel through the structure, giving rise to photonic bandgaps [19]. Any break in the symmetry across the structure will create a defect region, thereby causing a light mode to be pulled in to the bandgap. Because such a mode is forbidden from propagating in the bulk crystal, it is trapped and decays exponentially into the bulk, giving rise to a resonant mode [15, 19]. By changing the shape and size of the defect region, it is possible to tune the resonant frequency easily to any value within the bandgap.

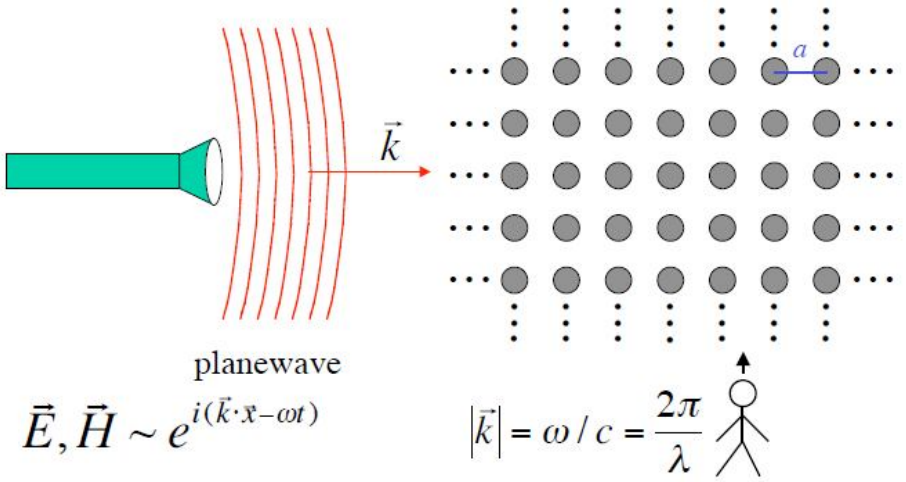

Figure 2.4 A schematic representation of a plane wave travelling through a photonic crystal. denotes the wave vector of the travelling wave.

Photonic crystal cavities typically have periodic holes drilled into bulk material to create the alternately repeating high and low dielectric constant regions. This type of arrangement of holes form the Bragg mirrors. By careful choice of the thickness of the intervening dielectric regions, reflectivity of different wavelengths of light can be regulated.

Typical photonic crystal cavities may possess single (H1 type – single hole missing from the center of the structure) [20] or multiple point (L3 type – three holes missing in a line) [21] defect regions offering 2D lateral confinement. These localized defects, intended to trap light, can contribute to high quality factors in the cavities. The defect region can also be extended to a row of missing holes, forming a waveguide cavity [22]. Depending on the nature of the bulk substrate, arrangement of the holes, their diameter and periodicities, a varied range of quality factors can be attained. Figure 2.5 shows instances of three different types of photonic cavities and their Q factors as observed.

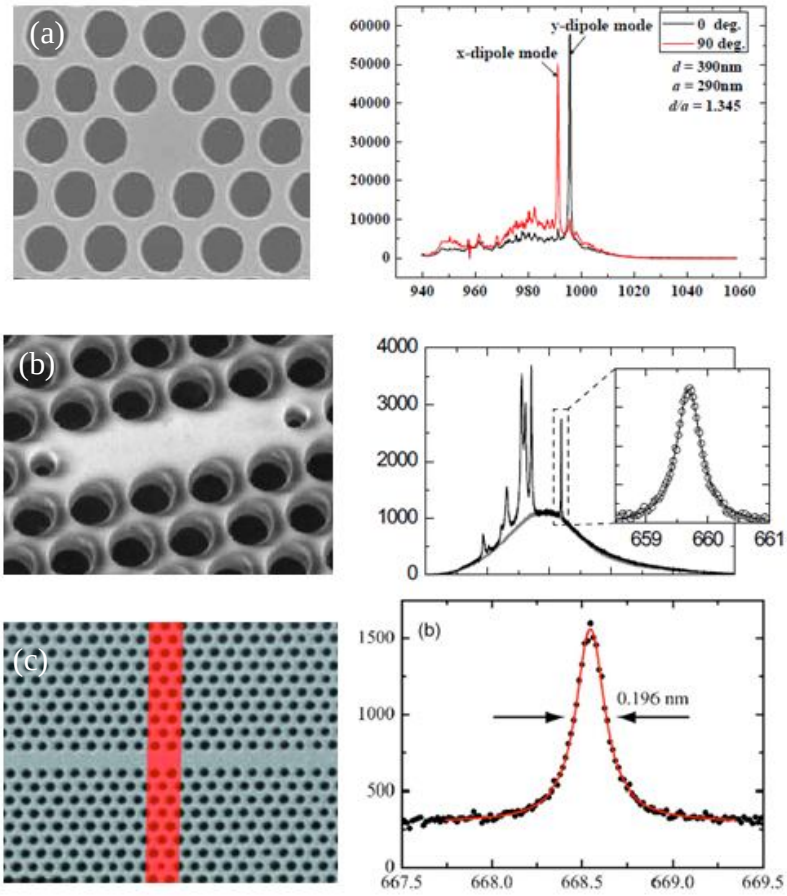

Figure 2.5 (a) H1 type photonic crystal cavity on GaAs substrate with an experimentally measured Q factor of ~3000 at a wavelength of ~995 nm [20]. (b) L3 type photonic crystal cavity on Silicon Nitride (Si_3N_4) substrate with resonant mode in the visible range. Q=1460 at ~660 [21]. (c) Double heterstrocture waveguide cavity on Si_3N_4 with Q=3411 at ~668.5 nm. Reprinted with permission from [22] ©2008 American Institute of Physics.

In addition to the photonic cavity types shown in Figure 2.5, a special type of photonic crystal cavity is a nanobeam cavity (see Figure 2.6(a)) [23]. Such cavities offer optical confinement by photonic crystal mirrors (Bragg mirrors) along the waveguide direction (x-pol in Figure 2.6(a)) and by total internal reflections on the transverse directions (y-pol in Figure 2.6(a)). For these cavities, the confined mode forms a hotspot at the center of the cavity. A four or seven-hole tapering is allowed on both sides of the center to allow loss-suppression by reducing the mismatch between the mirror and the waveguide [24]. Such design has led to observations of extremely high experimental quality factors.

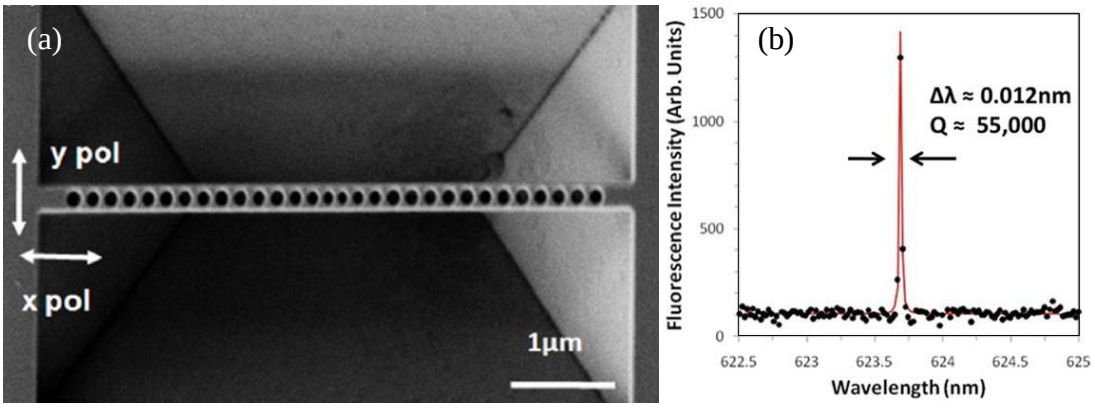

Figure 2.6 (a) A nanobeam photonic cavity with a four hole taper, fabricated on Silicon Nitride. (b) Fluorescence measurement performed on the cavity show a quality factor of ~55,000 at ~624 nm [23].

Although optical microcavities are adept at providing low-loss light confinement, they are not capable of doing so below a theoretical limit known as the effective mode volume, V_{eff}. V_{eff} is of the order of $\left(\lambda/n\right)^3$ for dielectric microcavities, where n is the refractive index of the material while λ is wavelength of the incident light [7]. Even though with certain types of photonic crystal cavities like nanobeam cavities, it has been possible to achieve mode volumes as low as $0.55\left(\frac{\lambda}{n}\right)^3$ [23], this still poses a certain limit to the Purcell enhancement [25] which is a determining factor in controlling spontaneous emission from single photon sources.

2.3. Purcell Effect

The rate of spontaneous emission from light sources depends on their environment. E.M. Purcell in 1946 introduced a revolutionary concept that the spontaneous emission of radiating dipoles can be tailored by placing them in a resonant cavity which helps modify the dipole field coupling and the density of the photon modes, thereby causing an enhancement in emission. This enhancement is given by the Purcell factor [25].

$$F_p = \frac{3}{4\pi^2}\left(\frac{\lambda}{n}\right)^3\left(\frac{Q}{V}\right) \tag{1}$$

where $\frac{\lambda}{n}$ is the wavelength within the material, while Q and V are the quality and the mode volume of the cavity respectively. From Eq.(1), it can be observed that if $V = V_{eff}$ (V_{eff} is the effective mode volume, as discussed in the previous Section) there is only a limited room for Purcell enhancement of emission from single photon sources. This gap can be bridged by using the properties of surface plasmons in addition to that of optical microcavities, e.g. photonic cavities.

2.4. Surface Plasmons

Surface plasmons are bound electromagnetic excitations at the interface between a metal (negative dielectric constant) and a dielectric (positive dielectric constant), resulting from collective electron oscillations at the surface of the metal [26]. These excitations propagate in a surface wave along the metal-dielectric interface, decaying exponentially in perpendicular direction on both sides of the interface.

We consider the plane metal dielectric interface ($z = 0$) as shown in Figure 2.7(a). The metallic medium is characterized by a complex frequency-dependent dielectric function $\varepsilon_1(\omega)$ while the dielectric medium has a real dielectric function $\varepsilon_2(\omega)$. The expression for surface plasmons, in this case, will be given by the solution of the Maxwell's equations localized at the interface. Expressed mathematically, it is the solution of the wave equation [26]:

$$\nabla \times \nabla \times E(r,\omega) = -\frac{\omega^2}{c^2}\varepsilon(r,\omega)E(r,\omega) = 0 \qquad (2)$$

In the above equation, $\varepsilon(r,\omega) = \varepsilon_1(\omega)$ when $z < 0$ and $\varepsilon(r,\omega) = \varepsilon_2(\omega)$ when $z > 0$. Since we are looking for homogeneous solutions (solutions that exist without external excitation) that decay exponentially with distance from the interface, we consider only p-polarized plane waves in both half spaces which can be written as:

$$E_i = \begin{pmatrix} E_{j,x} \\ 0 \\ E_{j,z} \end{pmatrix} e^{ik_x x - i\omega t} e^{ik_{j,z} z} \qquad j = 1,2 \qquad (3)$$

k_x and $k_{j,z}$ are the tangential and normal components of the transverse wave vector k (k the wavevector of light in vacuum and is expressed as $k = \frac{\omega}{c}$) such that:

$$k_x^2 + k_{j,z}^2 = \varepsilon_j k^2 \qquad j = 1,2 \tag{4}$$

In the absence of an external stimuli, $\nabla \bullet D = 0$, which allows us to write:

$$k_x E_{j,x} + k_{j,z} E_{j,z} = 0 \qquad j = 1,2 \tag{5}$$

Since the electric fields should be continuous across the interface of $z = 0$, it can be written that:

$$E_{1,x} - E_{2,x} = 0 \tag{6}$$

$$\varepsilon_1 E_{1,z} - \varepsilon_2 E_{2,z} = 0 \tag{7}$$

A solution exists for the system consisting of Eqs. (5), (6) and (7) only if either $k_x = 0$, which fails to explain the excitations travelling along the interface, or if

$$\varepsilon_1 k_{2,z} - \varepsilon_2 k_{1,z} = 0 \tag{8}$$

Using Eq.(8) in Eq.(4), k_x and $k_{j,z}$ can be derived as:

$$k_x = k\sqrt{\frac{\varepsilon_1 \varepsilon_2}{\varepsilon_1 + \varepsilon_2}} \tag{9}$$

$$k_{j,z} = k\sqrt{\frac{\varepsilon_j^2}{\varepsilon_1 + \varepsilon_2}} \tag{10}$$

From Eqs. (9) and (10), it can be observed that, k_x, the wave vector of surface plasmons in the direction of propagation, is real and is greater than the wave vector of light in vacuum (k). This is explained in the dispersion relation of surface plasmons in Figure 2.7(b) where $k_{spp} > k$. From the abovementioned Figure, it is clear that, since dispersion relation of light in vacuum (or in ambient air) does not intersect with the corresponding curve of surface plasmons, special momentum matching techniques have to be employed to couple light to surface plasmon mode.

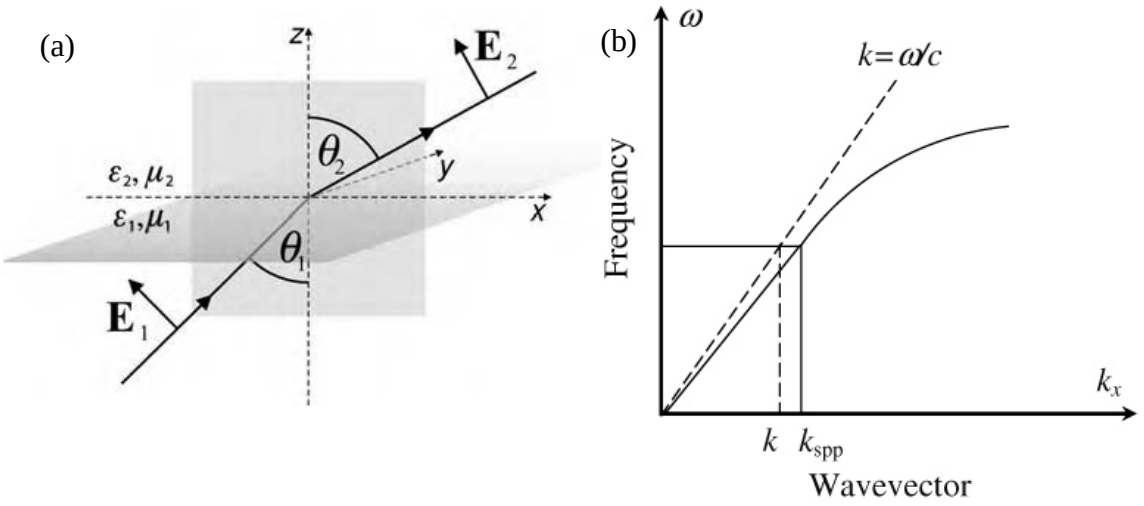

Figure 2.7 (a) Interface between two media (1 and 2) with separate dielectric functions [26]. (b) Dispersion curve of surface plasmons lies to the right of light line showing $k_{spp} > k$.

2.4.1 Localized Surface Plasmons

Localized surface plasmons are non-propagating excitations of electrons of metallic nanostructures coupled to an oscillating electromagnetic field [27]. The curved surface of the nanoparticles causes the electron oscillations to stay confined, thus leading to a resonance (called localized surface plasmon resonance) and consequently a field enhancement both inside and outside the particle (the latter in the near field zone only). This effect is most observable in gold and silver nanoparticles as their resonance falls into the visible region of the electromagnetic spectrum. Tuning the shape and size of the nanoparticles can shift their resonances to different wavelengths (shown in Figure 2.8(a)) of the spectrum, producing bright, vibrant colors in both transmitted and reflected light [28]. This property of localized surface plasmons has been long in use for stained glass windows and ornamental cups (Figure 2.8(b) and (c)).

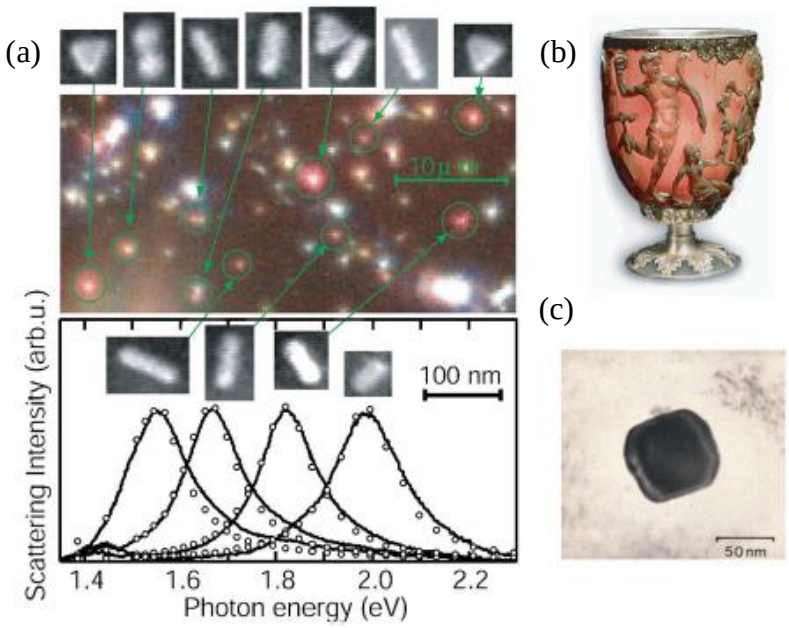

Figure 2.8 (a) Different shapes of gold nanoparticles produce different resonance spectra [28] (Reprinted with permission). (b) The Lycurgus glass cup, demonstrating the bright red color of gold nanocrystals in transmitted light (c) SEM image of a typical nanocrystal embedded in the glass (Courtesy: British museum). ©2005 American Institute of Physics

For particles with a diameter of $d << \lambda$, all the conduction electrons inside the particle oscillate in phase upon plane wave excitation of wavelength λ, leading to a build-up of polarization charges on the surface of the particle. These charges act as an effective restoring force, allowing for a resonance to occur at the particle dipole plasmon frequency, only with a $\pi/2$ phase lag with the driving frequency [27]. Thus a resonantly enhanced field builds up inside the particle, which is almost homogeneous inside the small volume of the particle. It also leads to enhanced absorption and scattering cross sections (described in details in Section 2.4.3) of the particle as well as enhanced local fields in its immediate vicinity.

2.4.2 Mode Volume of Plasmonic Cavities

To analyze the concept of mode volume in structures exhibiting plasmonic effects, let us consider first a simple example of a one dimensional plasmonic "nanoresonator" consisting of a thin dielectric layer sandwiched between two metal claddings (inset of

Figure 2.9(a)) [29]. Such a structure supports two propagating mode in the x direction, formed as a result of surface plasmonic effect, parallel to the metal interfaces. The lower order mode, which presents a symmetric distribution of the dominant electric field component E_z, is shown in the inset. In an analogy to the effective mode volume [30], an effective mode length, L_{eff}, can be chosen, such that L_{eff} is the ratio of the total energy of the surface plasmon mode to the energy per unit length, at a position of interest, which is usually the position of the greatest field.

Figure 2.9(a) shows that, for the lowest order mode propagating in the cavity, with decreasing dielectric gap size (normalized to free space wavelength λ), L_{eff} falls well below $\lambda/2$,which is the diffraction limit of light.

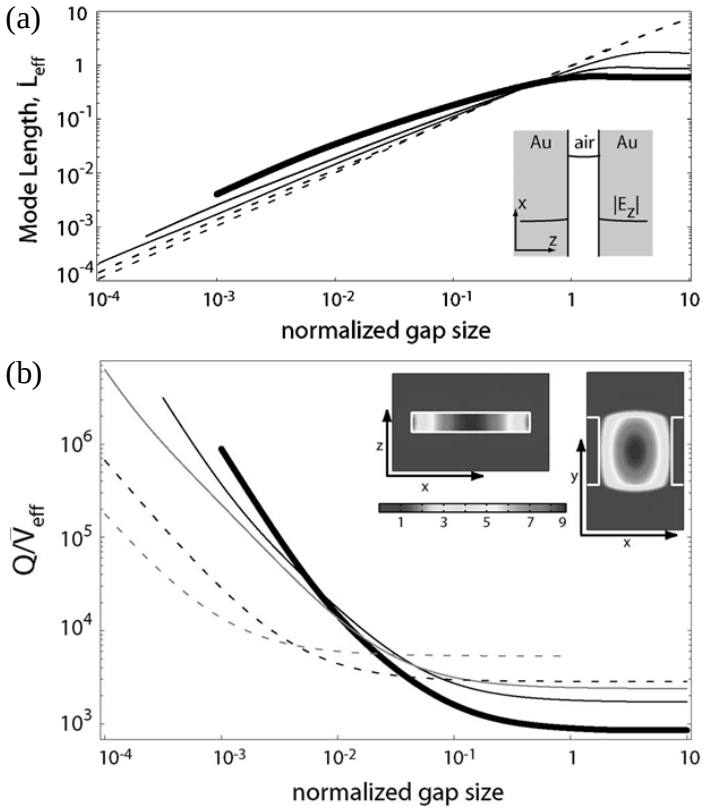

Figure 2.9 (a) The mode length of 1D plasmonic cavities can be made smaller than the diffraction limit of light by decreasing the cavity width. (b) Ratio of cavity quality to mode volume for a 3D plasmonic cavity increases exponetially with decreasing cavity width [29] (©2006 IEEE).

The above 1D resonator can be extended to a 3D cavity by adding reflective surfaces in the x direction (shown in Figure 2.9(b) inset), confining the propagation of the above mode to a finite cavity length L_x (thereby causing Fabry-Perot type oscillations). Assuming the walls to be perfect reflectors, the lowest order cavity mode will be excited when $L_x = \pi / k_x(\lambda, a)$ (k_x is the wave vector in the direction of propagation). Assuming a diffraction limited lateral resonator width of $L_y = \lambda / 2$, the cavity mode volume can be calculated to be [29]:

$$V_{eff} \sim L_{eff} \left(\frac{\pi\lambda}{2k_x} \right) \tag{11}$$

The quality factor of the cavity being mostly a function of dissipative losses from inside the metal (in absence of any radiative losses from the cavity), Q / V_{eff} increases greatly with decreasing gap size, as is shown by the above Figure 2.9(b). This effect can be attributed to the fact that V_{eff} decreases much faster than Q.

2.4.3 Losses in Metals

As seen in Figure 2.8(a), metal nanoparticles, because of their inherently lossy nature, possess very low quality factors (of the order of ~10). Losses in metals can be mainly accorded to *absorption* and *scattering* by the metal particles themselves. It can be said that, when metal particles are placed in the path of an incident beam, in a non-absorbing medium, these losses in the particles together result in the *extinction* of the beam (Figure 2.10(a)).

Let us consider the extinction caused by a single arbitrary particle placed in a non-absorbing medium and illuminated by a plane wave (refer to Figure 2.10(b)). Imagining a sphere of radius r around the particle, the rate at which electromagnetic energy crosses surface area A of the sphere is given by [31]:

$$W_A = -\int_A S \cdot \vec{e_r} dA \tag{12}$$

where S is the time-averaged Poynting vector [32]. Energy is absorbed by the particle only (as the medium is non-absorbing and therefore has no contribution) and is given by

$W_A > 0$. If W_S is the scattered energy rate across A, W_{ext} can be expressed as $W_{ext} = W_S + W_A$. Now, assuming the incident electric field to be x-polarized ($E_i = E\vec{e_x}$) for convenience's sake, in the far field region, where $r \to \infty$, W_{ext} is given by [31]:

$$W_{ext} = I_i \frac{4\pi}{k^2} \mathrm{Re}\left\{\left(X \cdot \vec{e_x}\right)_{\theta=0}\right\} \tag{13}$$

Here I_i is the incident irradiance and X is the vector scattering amplitude that depends on the direction of polarization (in this case, x-polarized). The ratio of W_{ext} to I_i, therefore, has the dimensions of an area, expressed by the extinction cross Section C_{ext}.Similarly, the absorption and scattering cross sections C_{abs} and C_{scat} are given by $\frac{W_{abs}}{I_i}$ and $\frac{W_{scat}}{I_i}$ respectively.

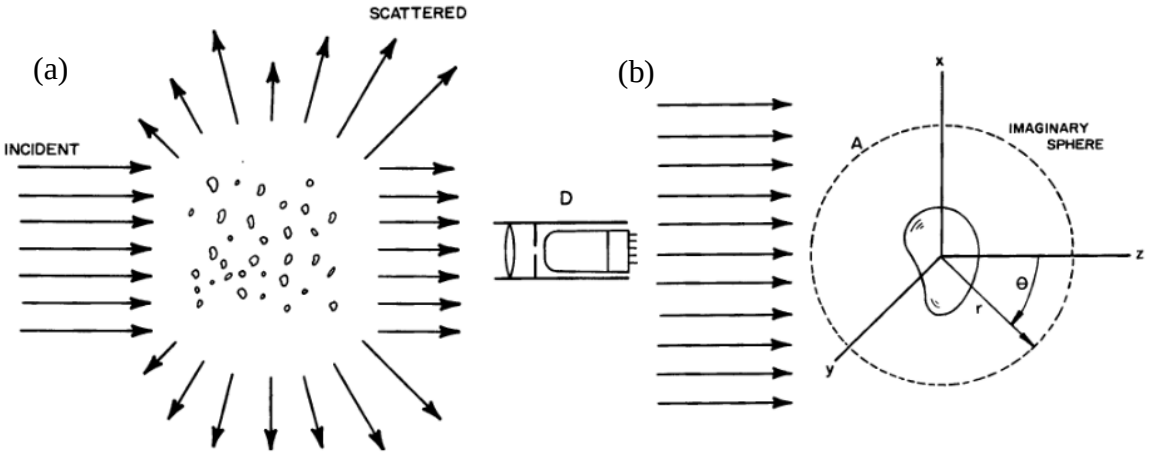

Figure 2.10 (a) Metal nanoparticles placed in the path of an incident beam absorb and scatter light, so that power of the beam received by detector D is less than the power of the incident beam. (b) A single metal particle in a non absorbing medium illuminated by a plane wave [31].

It is clear from Figure 2.9 that, using the properties of surface plasmons, light confinement to a mode volume smaller than the propagating wavelength can be achieved. This fact, coupled with the localized surface plasmonic effect, makes metallic nanoparticles a major candidate in overcoming the challenges posed by ordinary dielectric cavities to Purcell enhancement. As seen in Figure 2.8(a), however, metal

nanoparticles possess very low quality factors. Such poor qualities make them unsuitable for high-quality demanding applications alone. This led to the contemplation of a plasmonic-photonic hybrid approach, which has recently garnered a lot of interest.

2.5. Plasmonic-Photonic Hybrid Cavities

Hybrid plasmonic photonic cavities, created by combining dielectric photonic cavities with plasmonic particles, offer a compromise between high quality factors and high local field enhancement, where the best of both worlds are preserved to an extent. One of the earliest attempts at a hybrid approach was silver coating a whispering gallery mode microcavity [33]. In this case, although the results showed quite high quality factors, the confinement of the modes to the cavity microdisc was not very strong (Figure 2.11(a)). Further attempts included introducing upright metal nanowires to the center of a L3 cavity causing strong damping of the cavity mode (Figure 2.11(b)) [34].

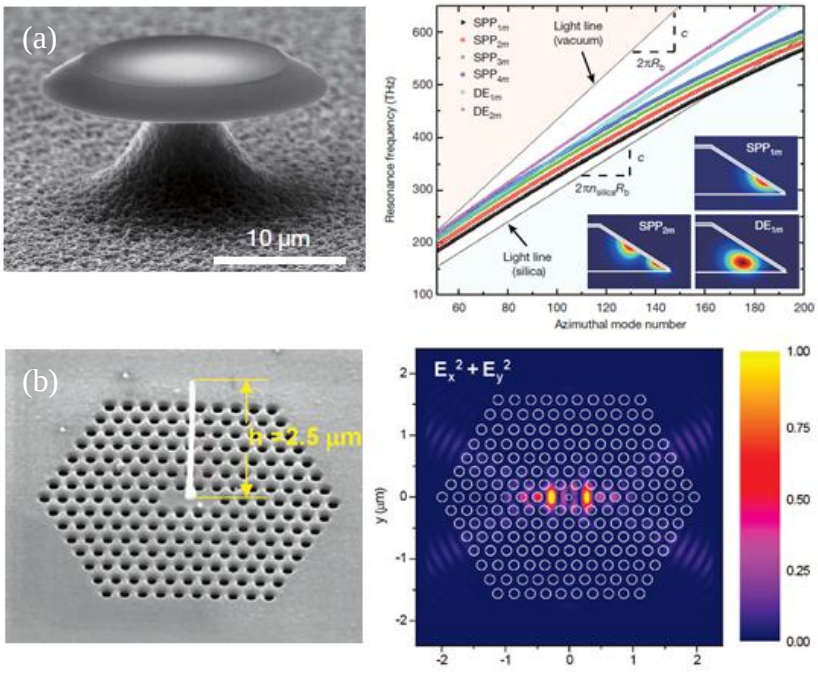

Figure 2.11 (a) SEM image of a fabricated silver-coated Surface Plasmon Polariton (SPP) microdisk resonator (left) and cavity mode dispersion curves for the resonator (right) showing the mode confinement hotspots (Reprinted by permission from MacMillan Publishers Ltd.: Nature ©2009) [33]. (b) SEM image of a photonic cavity with plasmonic nanoantenna at the center (left) and electric field profile of the cavity with the nanoantenna

at showing strongly damped cavity resonance mode (right). Reprinted with permission from [34] ©2008 American Chemical Society.

The latter approach was later modified and improved upon to achieve a design where the original cavity features are preserved and extended by the plasmonic characteristics. To accomplish this, a resonantly tuned metal nanoparticle is introduced into a photonic crystal cavity [35-37]. With such an approach, even though a certain loss in the quality is expected, it is limited to an agreeable value, while a substantial local field enhancement can be observed.

Figure 2.12 shows one such example of a hybrid photonic-plasmonic cavity. The double heterostructure cavity contains a line defect at the center. The cavity is fabricated from silicon nitride using electron beam lithography (EBL) technique and gold nanoparticles were selectively moved into place using dip pen technique with an AFM (atomic force microscope) tip [35]. The results reported, using one nanorod, showed that, depending on the orientation of the nanorod with respect to the cavity, the plasmonic resonance of the rods coupled to either of the two cavity modes, leading to enhanced emission peaks at the cavity resonances compared to that of bare cavities.

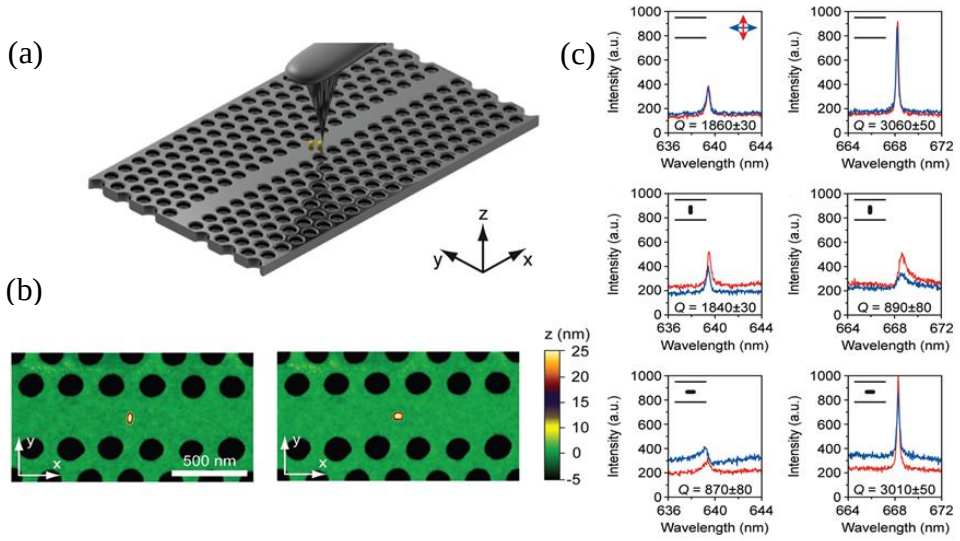

Figure 2.12 (a) Placement technique of gold nanoparticles in a double heterostructure photonic cavity using AFM tip. (b) AFM images of the cavity with a gold nanorod placed at the center in different orientations. (c) Resonance peaks of the two resonant modes of the

cavity (top), resonance peaks for the configuration shown in 2.12b-left (middle) and reosnance peaks for 2.12b-right (bottom). Red and blue curves refer to excitation polarizations perpendicular and parallel to the waveguide axis, respectively. Reprinted with permission from [35] ©2010 American Chemical Society.

2.5.1. Application to Single Photon Sources

Single photons offer great prospect in carrying information to test the secrecy of optical communications and could potentially be applied to the problem of sharing digital cryptographic keys [13, 38]. Although secure quantum-key-distribution systems based on weak laser pulses have already been realized for simple point-to-point links, true single-photon sources would improve their performance a great deal. Furthermore, these can also be used for quantum information processing and communication.

Single photon sources, simply speaking, are means for producing a series of regulated optical pulses, each of which contains one and only one photon. This particular property SPS can be utilized to a great advantage to build extremely secure and robust data communication systems. Since only one photon is transmitted at a time, any attempt to eavesdrop on the communication channel will result in total data loss.

SPS can be constructed using dielectric microcavities which help shape the directionality of emission of the photons. For example, quantum dots embedded in the microcavities shown in Figure 2.13 have measured single-photon emission rate of maximum 4.0 MHz with an extraction efficiency of 38% [13].

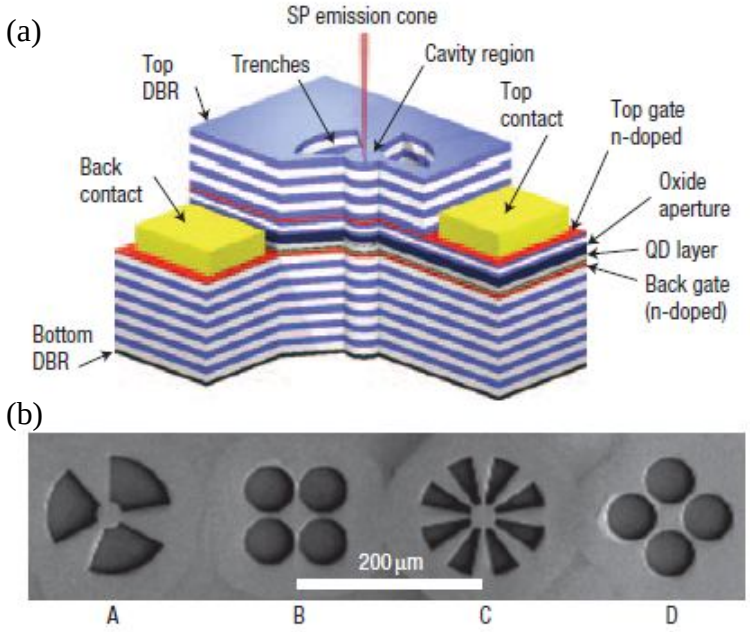

Figure 2.13 (a) A 3D schematic view of a single photon source containing a cavity region embedded between a 32-period bottom AlGaAs/GaAs DBR and a 23-period top DBR (white/blue layers). The cavity contains a single layer of InAs QDs (grey) and a mode-confining tapered AlOx region (dark blue). (b) Microcavities with various trench designs to control emission from embedded quantum dot emitters. Reprinted by permission from MacMillan Publishers Ltd.: Nature Photonics ©2007 [13].

Further enhanced directivities have been attempted with quantum dots placed on the feed element of a metal Yagi-Uda nanoantenna (Figure 2.14) [39]. Although, this design does improve directionality of emission, the effect of surface plasmons tends to make the arrangement lossy. Under these conditions, a hybrid solution, like that of plasmonic-photonic cavities, could be one of the best ways of approach.

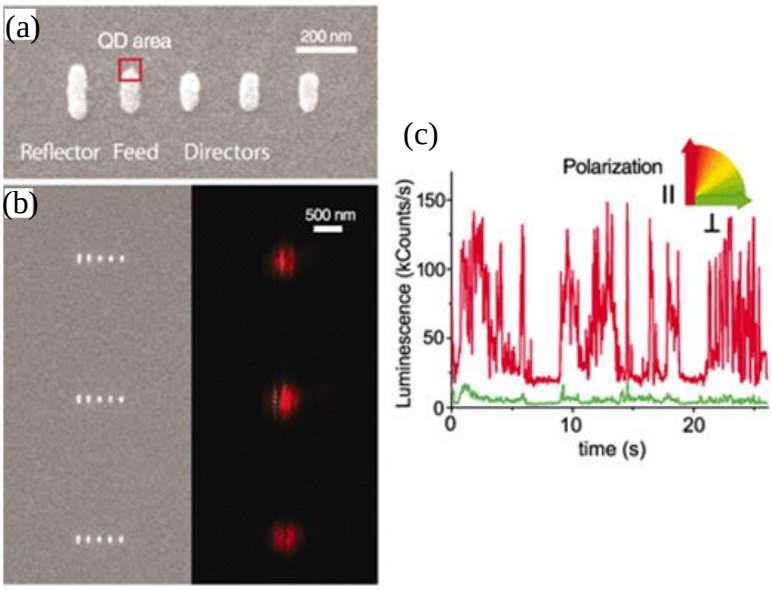

Figure 2.14 (a) SEM image of fabricated five-element Yagi-Uda antenna consisting of a feed element, one reflector, and three directors. A QD is attached to one end of the feed element (marked in red). (b) Comparison of SEM and scanning confocal luminescence microscopy images of three antennas driven by QDs. (c) Intensity time trace of luminescence in two different polarizations for one of the antennas in 2.14b, showing blinking of a single QD [39] (Reprinted with permission from AAAS).

2.6. Theoretical modeling of hybrid cavities

So far, photonic crystals have been comprehensively analyzed using techniques like finite difference time domain (FDTD), relying on brute force calculations for the entire cavity. For hybrid cavities as discussed in previous Section, changing the shape of the cavity or changing the metal particle requires a repeat computation, and there consumes a significant amount of computation time and memory [40, 41].

To solve this problem, a hybrid approach based on perturbation theory can be taken. In this approach, the fields of the bare cavity are calculated, followed by a separate calculation of the local fields of the plasmonic particle on the waveguide (without the cavity), and the contributions from both the global and local fields are combined to obtain the changed frequency as well as the quality factor due to the introduction of the nanoparticle.

Unlike comprehensive simulation techniques, perturbation theory offers physical insight related to the hybrid approach by splitting up the problem naturally and

considering the cavity and local field effects separately. Multiple designs with different nanoparticles can be pursued with recalculations needed for only the local part. Similarly, if different cavities are chosen with the same local contribution from a particular nanoparticle, then only the cavity calculation need be repeated. Overall, this results in a faster design process.

2.6.1. Perturbation Theory

We consider E_1 and H_1 as the electric and magnetic fields respectively, in an unperturbed cavity with perfectly conducting walls and a resonant frequency ω , such that:

$$E = E_1 e^{j\omega t} \tag{14}$$

$$H = H_1 e^{j\omega t} \tag{15}$$

Then, we can write D_1 and B_1 as:

$$D_1 = \varepsilon_0 \varepsilon_1 E_1 \tag{16}$$

$$B_1 = \mu_0 \mu_1 H_1 \tag{17}$$

where ε_0 and μ_0 denote absolute permittivity and absolute permeability while ε_1 and μ_1 denote relative permittivity and permeability values of the cavity. On introducing a particle (perturbation) into the cavity, the electric and magnetic fields in the cavity undergo a change, thus changing the resonant frequency ($\omega + \delta\omega$). The field expressions for the perturbed cavity can be given as [42]:

$$E' = (E_1 + E_2) e^{j(\omega+\delta\omega)t} \tag{18}$$

$$H' = (H_1 + H_2) e^{j(\omega+\delta\omega)t} \tag{19}$$

where E_2 and H_2 are the corrections to the field from the perturbation. Assuming ε_2 and μ_2 to be the relative permittivity and permeability of the perturbing particle respectively, D_2 and B_2 can be written as:

$$D_2 = \varepsilon_0 [\varepsilon_2 (E_1 + E_2) - \varepsilon_1 E_1] \tag{20}$$

$$B_2 = \mu_0 [\mu_2 (H_1 + H_2) - \mu_1 H_1] \tag{21}$$

From Maxwell's differential equations, we can derive from Eqs. (15) and (19):

$$\nabla \times E_1 = -j\omega B_1 \tag{22}$$

$$\nabla \times E_2 = -j\left\{\omega B_2 + \delta\omega\left(B_1 + B_2\right)\right\} \tag{23}$$

Similarly, the expressions for magnetic fields can be derived from Eqs.(16) and (20):

$$\nabla \times H_1 = j\omega D_1 \tag{24}$$

$$\nabla \times H_2 = j\left\{\omega D_2 + \delta\omega\left(D_1 + D_2\right)\right\} \tag{25}$$

Now we use the vector identity

$$div\left\{\left(H_1 \times E_2\right) + \left(E_1 \times H_2\right)\right\} = E_2.\nabla \times H_1 - H_1.\nabla \times E_2 + H_2.\nabla \times E_1 - E_1.\nabla \times H_2,$$

which can be rewritten putting $\frac{\delta}{\delta t} = j\omega$ as:

$$\begin{aligned} &H_1.\nabla \times E_2 + E_1.\nabla \times H_2 = \\ &j\omega E_2.D_1 - j\omega H_2.B_1 - div\left\{\left(H_1 \times E_2\right) + \left(E_1 \times H_2\right)\right\} \end{aligned} \tag{26}$$

Using Eqs. (23) through (25), the right side of the above Eq. (26) can also be expressed as:

$$\begin{aligned} &H_1.\nabla \times E_2 + E_1.\nabla \times H_2 = \\ &j\omega\left\{E_1.D_2 - H_1.B_2\right\} + j\delta\omega\left\{(E_1.D_1 - H_1.B_1) + (E_1.D_2 - H_1.B_2)\right\} \end{aligned} \tag{27}$$

Substituting Eq. (26) to (27) and integrating over the volume V_1 of the cavity after some rearrangement, we obtain:

$$\begin{aligned} &j\delta\omega\iiint_{V_1}\left\{\left(E_1.D_1 - H_1.B_1\right) + \left(E_1.D_2 - H_1.B_2\right)\right\}dV = \\ &j\omega\iiint_{V_1}\left\{\left(E_2.D_1 - E_1.D_2\right) - \left(H_2.B_1 - H_1.B_2\right)\right\}dV - \\ &\iiint_{V_1} div\left\{\left(H_1 \times E_2\right) + \left(E_1 \times H_2\right)\right\}dV \end{aligned} \tag{28}$$

If S_1 is the surface enclosing V_1, the divergence integral of the above equation can be replaced by the divergence theorem so that:

$$\begin{aligned} &j\delta\omega\iiint_{V_1}\left\{\left(E_1.D_1 - H_1.B_1\right) + \left(E_1.D_2 - H_1.B_2\right)\right\}dV = \\ &j\omega\iiint_{V_1}\left\{\left(E_2.D_1 - E_1.D_2\right) - \left(H_2.B_1 - H_1.B_2\right)\right\}dV - \iint_{S_1}\left\{\left(H_1 \times E_2\right) + \left(E_1 \times H_2\right)\right\}.dS \end{aligned} \tag{29}$$

For the introduction of a small particle of volume V_2, the relative change in frequency, $\delta\omega$, in V_1 with respect to the cavity resonant frequency ω is now given by:

$$\frac{\delta\omega}{\omega} = \frac{\iiint_{V_2} \{(E_2.D_1 - E_1.D_2) - (H_2.B_1 - H_1.B_2)\} dV - \frac{1}{j\omega} \iint_{S_1} \{(H_1 \times E_2) + (E_1 \times H_2)\}.dS}{\iiint_{V_1} (E_1.D_1 - H_1.B_1) + (E_1.D_2 - H_1.B_2)\, dV} \quad (30)$$

The most common forms of this perturbation formula have been derived for cavities with perfectly conducting walls, in case of which, the surface integral term vanishes [42]. In a dielectric waveguide with non-conducting walls, however, there would be some energy flow through the waveguide which cannot be accounted for if surface integral is assumed to be zero. It is also commonly assumed that since D_2 and B_2 are much smaller than D_1 and B_1 respectively (as particle size V_2 << cavity volume V_1), the contribution of the second integral in the denominator may be neglected except in the neighbourhood of the particle [42, 43]. To achieve higher accuracy in results, this assumption may be neglected.

Clearly $\frac{\delta\omega}{\omega}$ obtained from Eq. (30) is a complex term in the presence of loss. Now, assuming Ω to be the complex resonance frequency and Q_1 to be the quality factor of the unperturbed cavity Ω can be expressed as:

$$\Omega = \omega\left(1 + \frac{j}{2Q_1}\right) \quad (31)$$

The complex resonance frequency of the perturbed cavity with a new resonance of $Q_a^{'}$ can therefore be written as:

$$\Omega + \delta\Omega = (\omega + \delta\omega)\left(1 + \frac{j}{2Q_a^{'}}\right) \quad (32)$$

Using Eqs. (31) and (32), we can separate $\frac{\delta\omega}{\omega}$ obtained from Eq. (31) in its real and imaginary components with the following expression [42]:

$$\frac{\delta\Omega}{\omega} = \frac{\delta\omega'}{\omega} + j\left\{\frac{1}{2Q_a^{'}} - \frac{1}{2Q_1}\right\} \quad (33)$$

From Eq. (33), it is clear that the real part of the expression obtained from Eq. (30) (written as $\frac{\delta\omega'}{\omega}$ for convenience) gives the frequency shift, whereas the imaginary part

(that we can write as $\frac{\delta\omega''}{\omega}$) gives the new quality factor. Using Eq. (33), we can therefore write the new quality factor of the perturbed cavity as:

$$Q_a' = \frac{\omega}{2\left(\delta\omega'' + \frac{\omega}{2Q_1}\right)} \tag{34}$$

Figure 2.15 shows a 2D cavity with perfectly conducting walls. E_1 is electric field within the unperturbed cavity while E' is the electric field after the introduction of the perturbing sphere (depicted in grey).

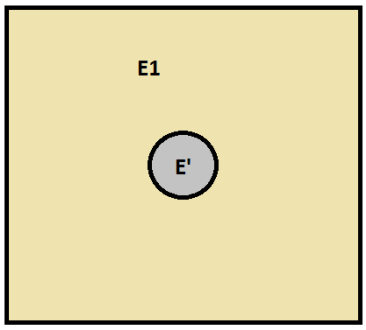

Figure 2.15 Electric field distribution in the neighbourhood of a dielectric sphere, the field being uniform and equal to E1 in the absence of the sphere.

2.7. Summary

In this Chapter we discussed the concept and applications of dielectric optical microcavities, their different types and performances. Various properties of surface plasmons that help them complement the short comings of dielectric cavities are introduced. It was shown that previous works have successfully realized a combination of the two, with good results. Such hybrid microcavities find important applications, specifically in single photon sources and more broadly in quantum encryption systems and enhanced laser sources. It is further proposed that theoretical modeling of such cavities can be performed without resorting to a comprehensive simulation technique (FDTD).

3. Nanofabrication, Measurement and Design Techniques

3.1. Introduction

This Chapter provides an overview of the various nanofabrication technologies, measurement and theoretical design techniques used throughout my research. It also enumerates the most important aspects that need to be taken care of in each of them to prevent unwanted results. Outcomes of application of these technologies to my work are discussed in the next Chapter.

3.2. Scanning Electron Microscopy

A Scanning Electron Microscope is an instrument that scans the sample surface with a finely converged electron beam in vacuum, detects the information produced at that time from the sample and presents an enlarged image of the sample surface on the monitor screen.

By irradiating the sample with an electron beam in vacuum, various signals from a substrate like secondary electrons, backscattered electrons, transmitted electrons, characteristic x-rays etc. are generated. The SEM mainly utilizes the secondary electrons or back scattered electron signals to form an image. As secondary electrons are produced near the sample surface, they reflect the fine topographical structure of the sample [44].

Figure 3.1(a) shows a Hitachi S-4800 SEM that has been used for imaging the experimental works described in Section 4. Figure 3.1(b) shows the different types of information that can be gathered from a substrate under SEM observation.

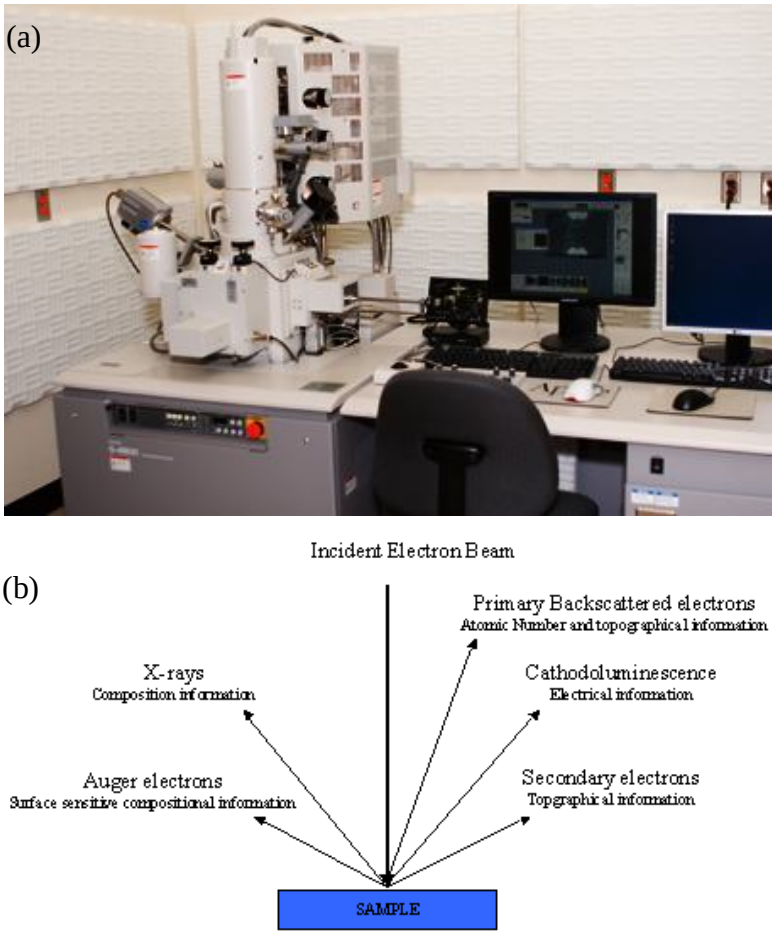

Figure 3.1 (a) Hitachi S-4800 SEM at the Advanced Microscopy Facility at UVic (Courtesy: Uvic AM Facility website). (b) Different types of information about a sample that can be obtained from SEM.

3.2.1. Working Principle

SEM utilizes electrons in the formation of a microscopic image. The electrons are usually emitted from a tungsten filament that is heated by running a current through it. The emitted electrons are accelerated towards the sample with a high potential difference, and focused to a certain spot with electromagnetic lenses. Electromagnetic fields are also used for scanning the beam across the area of the sample being imaged. The actual image is formed by detecting secondary electrons resulting from the collision of the primary electron beam with the sample surface. The primary electrons supply energy to the electrons in the surface of the sample that are, in turn, emitted and detected. Some of the primary electrons are backscattered and detected. The image formed by backscattered

electrons has variations in brightness, since heavier elements backscatter electrons more efficiently due to their larger size.

Due to the interaction process with the primary electrons, many sample atoms are left in an excited state. When these atoms return to a lower energy state, they emit either Auger electrons (more common with light elements) or X-rays (more common with heavy elements) that provide information on the chemical composition of the sample.

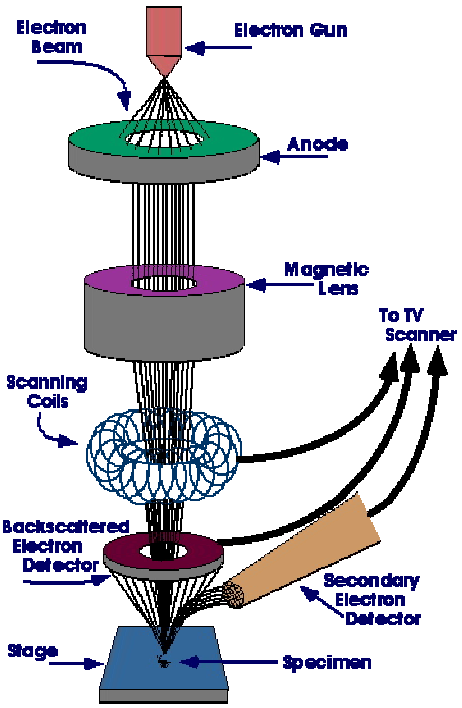

Figure 3.2 Sample irradiation by electron beam inside SEM column.

3.2.2. Imaging Instabilities

Often SEM imaging can get difficult. Images may move or fluctuate and may even be distorted. Sample structural details may be blurry, brightness may be unstable, images may be hard to bring into focus. Probable causes, normally, are charge-up phenomenon, sample contamination, beam damage and effect of external disturbances.

Charge-up phenomenon: In an electron beam irradiation area on a conductive sample surface, the incoming electron flow is counterbalanced by the outgoing electron flow. But for non-conductive samples, these two are not equal. Because of unbalanced changes,

surface potential will vary and charge-up will appear. This is particularly conspicuous when scan speed or magnification is changed.

Charge-up can be controlled largely by creating a conducting path for non-conductive samples (such as, applying a metal coating on the sample and connecting it to the metal sample stage, using a conductive paste) and using rapid raster scans rather than slower.

Sample contamination: The phenomenon by which gas molecules of hydrocarbons existing around the sample, collect on the sample due to electron beam irradiation, then bond together and adhere to the sample surface is referred as contamination. The clarity of the image at the area of exposure decreases and becomes darker. The darkness is likely because of the matter that accumulates on the sample surface and suppresses the discharge of secondary electrons from the sample.

Sample contamination can be reduced by using a minimum amount of conductive paste or tape while mounting the sample. The paste must be made sure to dry before inserting the sample to the specimen chamber. Focussing should be carried out as quickly as possible and observing the same location for a long time, especially at high magnification, must be avoided.

Beam damage: Thermal or chemical changes occuring on a sample due to electron beam irradiation, are attributed to beam damage. Polymeric materials and biological samples are susceptible to heat and may be readily damaged by the electron beam.

Beam damage can be minimized by reducing the sample irradiation current, accleration voltage, and improving the heat conductivity by metal-coating it.

External disturbances: Fringes and distortions may appear on a SEM profile due to noise vibrations and stray magnetic fields. To prevent this, the microscope must be installed away from air-conditioners, pumps, transformers or large capacity power cables.

Some other causes of image abnormalities are:

1. Moving sample because it was not properly fixed to the sample stage, specimen holder screw was not tightened properly or sample was inserted incompletely on the specimen stage.
2. Unfocussed image because of inadequate optical alignment, smaller or larger than necessary working distances.

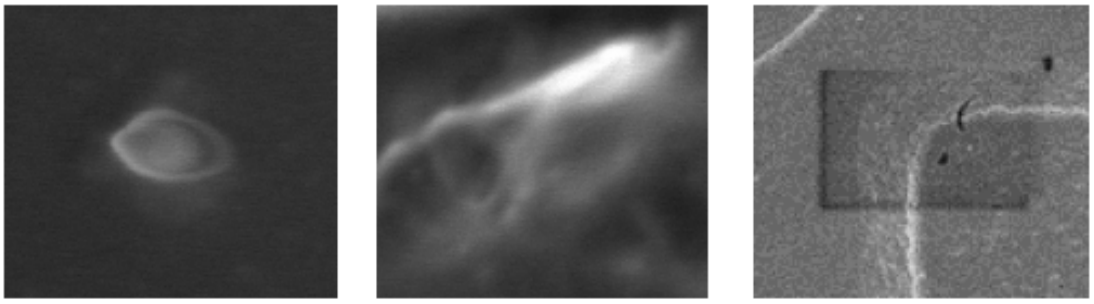

Figure 3.3 (a) Distorted image due to charging (b) uneven image brightness (c) sample contamination

3.2.3. Energy Dispersive X-ray Spectroscopy

An energy dispersive X-ray spectrometer (EDX or EDS) consists of a solid state X-ray detector that detects the X-rays generated by irradiating the sample surface with an electron beam (Figure 3.1). It also consists of a multi-channel pulse analyzer, and together with a Solid State Detector (SSD), is used to analyze the elemental composition of any sample. In EDX mode, samples are imaged using back scattered electrons instead of secondary electrons that are used in the primary imaging mode.

Certain parameter adjustments have to be made in the SEM before it can be used to observe X-rays. The most notable among these are, decreasing the sample working distance and increasing the electron beam acceleration voltage. The most advantageous aspect of EDX is that no matter how many layers of other elements have been piled on, the traces of a particular element, if it exists in the sample, will always be detected.

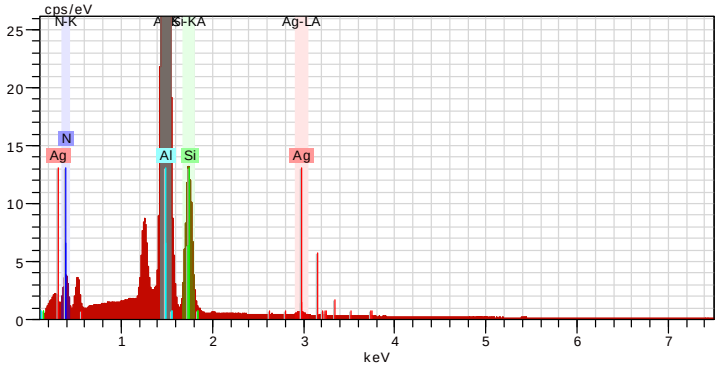

Figure 3.4 EDX pulse analyzer output detecting the presence of silver (Ag), silicon nitride (Si, N) and aluminum (Al- from the sample stage) in a given sample.

3.3. Focussed Ion Beam Milling

Focused ion beam, also known as FIB, is a technique used particularly in the semiconductor and materials science fields for site-specific analysis, deposition, and ablation of materials. However, while the SEM uses a focused beam of electrons to image the sample in the chamber, a FIB setup instead uses a focused beam of ions, e.g., Gallium ions. This is because FIB is mostly used as a micro machining tool. Ions are much heavier than electrons and are therefore capable of gaining much higher momentum. Being larger, they also cannot penetrate individual atoms of the sample, thus causing little change to the latter's characterization.

FIB can also be used to deposit materials, like Tungsten, on a sample. This is useful, as the deposited metal can be used as a sacrificial layer, to protect the underlying sample from the destructive sputtering of the beam.

Figure 3.5 Hitachi FB-2100 FIB at Advanced Microscopy Facility at UVic (Courtesy: Uvic AM Facility website).

3.3.1. Working Principle

Most widespread FIB instruments use Liquid-Metal Ion Sources (LMIS), especially Gallium ion sources. In a Gallium LMIS, gallium metal is placed in contact with a tungsten needle and heated. Gallium wets the tungsten, and a huge electric field (greater than 10^8 volts per centimeter) causes ionization and field emission of the Gallium atoms. Source ions are then accelerated to 5-50 keV and focused onto the sample

by electrostatic lenses. LMIS produce high current density ion beams with very small energy spread.

The Gallium (Ga+) primary ion beam hits the sample surface and sputters a small amount of material, which leaves the surface as either secondary ions or neutral atoms. The primary beam also produces secondary electrons. As the primary beam rasters on the sample surface, the signal from the sputtered ions or secondary electrons is collected to form an image.

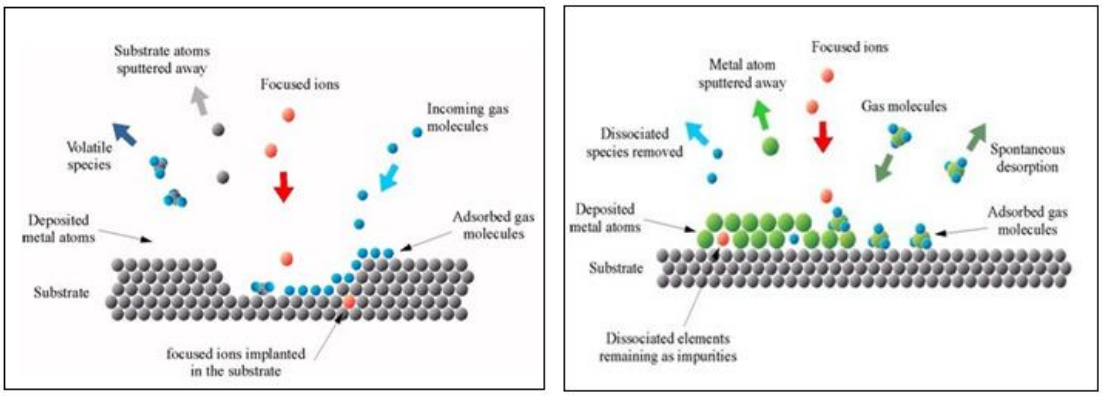

Figure 3.6 Sputtering (left) and deposition (right) with FIB

At low primary beam currents, a small amount of material is sputtered and modern FIB systems can easily achieve ~5 nm imaging resolution. At higher primary currents, a great deal of material can be removed by sputtering, allowing precision milling of the specimen down to a sub micrometer scale.

3.3.2. Fabrication Concerns

FIB fabrication presents many challenges that need to be overcome in order to achieve a decently performing device. Often, more than one beam, varying in acceleration voltages and current densities, are required to meet the needs. Moreover, FIB does not agree well with nonconductive or even semi conductive surfaces. But compared to other fabrication methods (electron beam lithography, photolithography or chemical etching), if the pattern to be fabricated is small, it offers much greater resolution and much shorter fabrication time.

Beam selection: Depending on the nature of the substrate and the delicacy of the structures to be fabricated, beam selection is the most important step in FIB milling. Ion

beams can vary in current density, acceleration voltage and aperture size, offering a wide selection for either bulk material removal or precision cutting. For a given beam, current density can be increased further (by about four times) by turning on the condenser lens. The higher the beam current, the more destructive it is and lesser is the resolution.

Beam alignment: If more than one beam is to be used, it needs to be made sure that all of these are aligned at the same point. Without a near perfect alignment, cuts can go badly off-position. Focusing and alignment have to be completed as quickly as possible (just like SEM) to avoid the beam eating into the sample. This is particularly critical when aligning the more destructive beams at high magnification.

Sample charging: Although FIB is less affected by sample charge-up than SEM, it still can be a big challenge if the structures to be fabricated are precise and delicate while the sample is semi or non-conductive. Workarounds can be made to increase conductivity (depositing tungsten wires, for example). Beams may need realignment frequently and even at very short spatial intervals, if multiple structures are being fabricated.

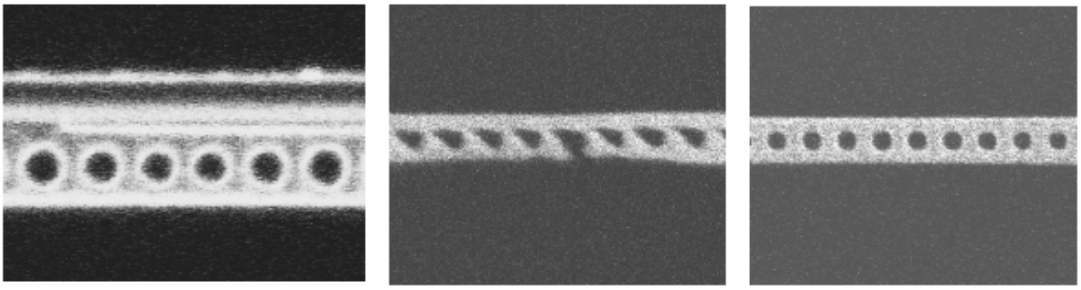

Figure 3.7 (a) Poor selection of beam caused insufficient material removal from the top of the fabricated structure. (b) Badly aligned beam damaged the shape of the holes. (c) Well aligned beam resulted in circular holes.

3.4. Fluorescence Microscopy

Fluorescence microscopy is based on the phenomenon that certain materials emit energy that is detectable as visible light when irradiated with the light of a specific wavelength (fluorescence). The sample is illuminated with a light source (lasers, for example) that excites fluorescence (Figure 3.8). The fluoresced light, which is usually at a longer wavelength than the illumination, is collected, in reflection mode, through a microscope objective and detected, usually with a CCD. Just before detection, the weak fluorescence emitted from the sample is separated from the much brighter excitation light

using a filter (emission filter). If a broadband source instead of a laser is used, a second filter that only lets through radiation with the specific wavelength that matches the fluorescing sample (excitation filter) is added in front of the source (Figure 3.8).

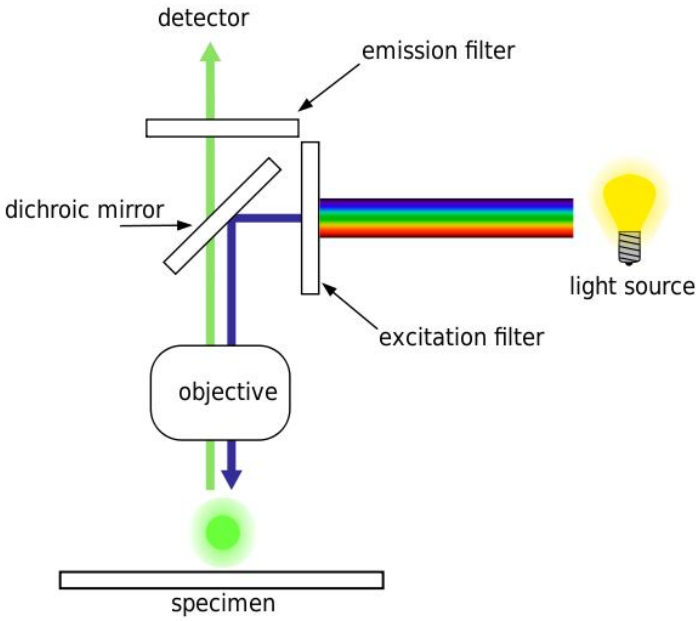

Figure 3.8 A fluorescence microscope setup

3.5. Finite Difference Time Domain (FDTD) Modelling

FDTD is an algorithm used for modeling a wide variety of applications that involve propagation of electromagnetic radiation through complicated media. Simply speaking, time-dependent Maxwell's equations (in partial differential form) are discretized using central difference approximations to the space and time partial derivatives [45]. The resulting finite-difference equations are solved separately: first, the electric field vector components in a volume of space are solved at some given instant of time (say, t), then the magnetic field vector components in the same spatial volume are solved at the next instant of time ($t+\Delta t$); and the process is repeated until the desired steady-state electromagnetic field behavior is reached.

In order to use FDTD, a computational domain must be established. The computational domain is simply the physical region over which the simulation will be performed. The electric (E) and magnetic fields (H) are determined at every point in space within this domain. The material of each cell within the domain must be specified. Typically, the

material is either free-space (air), metal, or dielectric. Any material can be used as long as the permeability, permittivity, and conductivity are specified.

Once the computational domain and the grid materials are established, a source is specified. The source can be an impinging plane wave, a current on a wire, or an applied electric field, depending on the application.

Since the E and H fields are determined directly, the output of the simulation is usually the E or H field at a point or a series of points within the computational domain. The simulation evolves the E and H fields forward in time. Processing may be done on the E and H fields returned by the simulation. Data processing may also occur while the simulation is ongoing.

While the FDTD technique computes electromagnetic fields within a compact spatial region, scattered and/or radiated far fields can be obtained via near-to-far-field transformations.

3.5.1. Computational Domain & Materials

The entire 3D computational domain comprises of small 3D cells that gives the domain a meshed look. For each of these mesh points (cells), finite difference equations are solved. The most fundamental simulation quantities like material properties and geometrical information, electric and magnetic fields are calculated at each mesh point. The mesh discretizes the structure to be simulated (Figure 3.9). Therefore, for curved surfaces, the smaller the mesh is, the more accurately the actual shape of the underlying structure can be represented.

Since the standard FDTD algorithm performs discretization onto a Cartesian mesh, if each mesh cell in the simulation region has the same volume, smaller mesh size also means longer simulation times and larger computational memory requirements. Moreover, Cartesian meshing is unable to account for structure variations that occur within any single mesh cell, resulting in a mesh of ‘staircase’ permittivity.

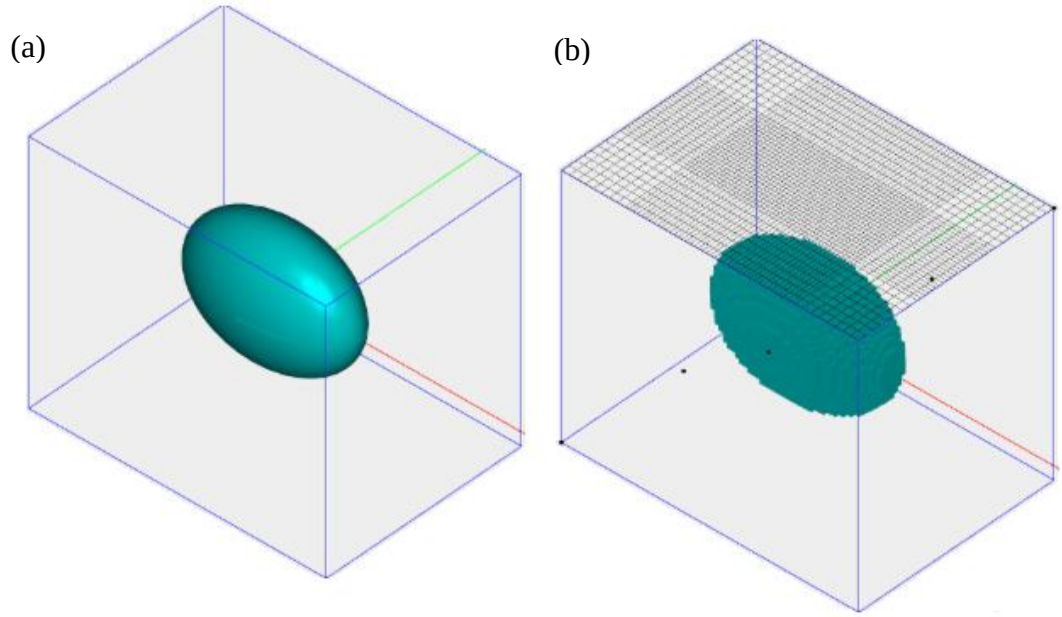

Figure 3.9 (a) Actual shape of the structure to be simulated. (b) Structure discretized with 5 nm size mesh.

Conformal mesh: Conformal mesh methods try to account for subcell features by solving Maxwell's integral equations near structure boundaries [46]. This allows the boundaries to be better represented even when using a coarse FDTD mesh on the rest of the structure. This enhances simulation accuracy for a given mesh size and therefore makes it possible to run shorter simulations without sacrificing accuracy.

Graded mesh: The FDTD algorithm supports a graded mesh of Cartesian cells. This means that the size of the mesh cells can vary as a function of position throughout the simulation region [47]. Many optical structures have properties that are critically sensitive to the precise locations of material interfaces. This is particularly true of structures that have resonant characteristics or have high refractive index contrast at the interfaces. The non-uniform mesh makes it possible to take into account the precise geometric location of these interfaces by using fine mesh cells in regions where the interfaces are important, and larger mesh cells in bulk regions where there are no important interfaces, e.g., homogeneous areas, thereby requiring less memory and less computation time than a comparable uniform mesh.

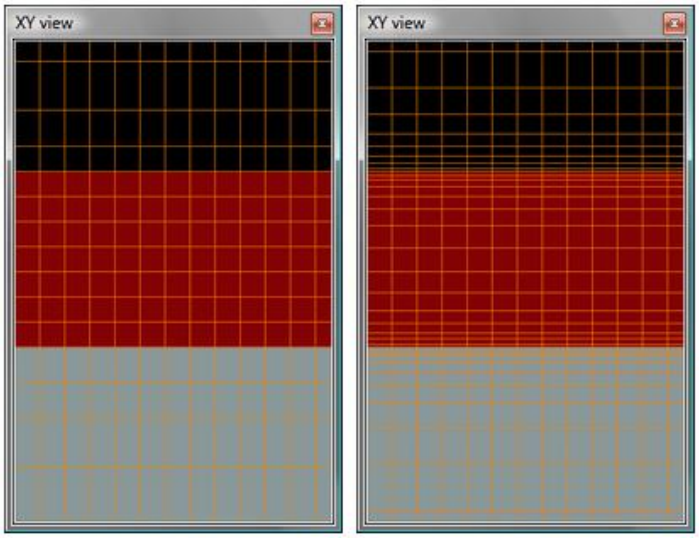

Figure 3.10 Graded mesh uses finer mesh cells near the interfaces and larger mesh cells in the bulk region (right) which reduces memory and computation time requirements than uniform mesh (left)

Boundary conditions: When electromagnetic field equations are solved using finite-difference techniques in unbounded space, the domain in which the fields are calculated must be limited in some way. This is necessary to store the computed data in the limited storage space of computers. By truncating the mesh and using absorbing boundary conditions, this objective can be achieved [48].

a) Perfectly matched layer (PML): PML boundaries absorb electromagnetic energy incident upon them [49]. PML is most effective when absorbing radiation at normal incidence, but can have significant reflection at grazing incidence.

b) Perfect electric conductor (PEC): PEC or metal boundary conditions are used to specify boundaries which are perfectly reflecting, allowing no energy to escape the simulation volume along that boundary.

Material fitting: Materials with complex permittivities like metals have variable dieelctric functions within a given wavelength range, as detailed in Section 2.4. Results may be erroneous in the absence of a good fit between the FDTD model for a source wavelength range and the actual material permittivity for that range. The quality of the fit can be adjusted by varying different parameters like the ratio of weightage assigned to the

real and imaginary parts of the dielectric function, fit tolerance and the number of coefficients used in the fit plot.

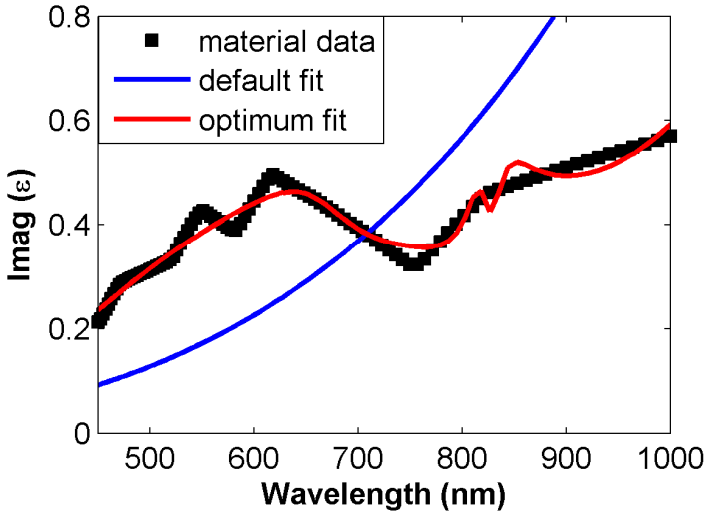

Figure 3.11 Comparison between default fit of the FDTD model to the complex material data and an optimum fit that can be obtained by adjusting fit parameters

3.5.2. Sources

Sources with different types of electromagnetic behaviours can be used for simulations. For example, oscillating dipoles act as radiating point sources of electromagnetic fields. Dipoles can be placed at one or more points in the simulation area. Plane wave sources, on the other hand, are used to inject laterally-uniform electromagnetic energy from one side of the source region. Broadband plane waves (with multiple modes) can be modified to inject a single guided mode in a simulation region (termed as mode source).

Figure 3.12(a) shows a mode source injected at one end of a photonic nanobeam cavity that acts as a waveguide. 3.12(b) shows an electric dipole source at the center of the nanobeam.

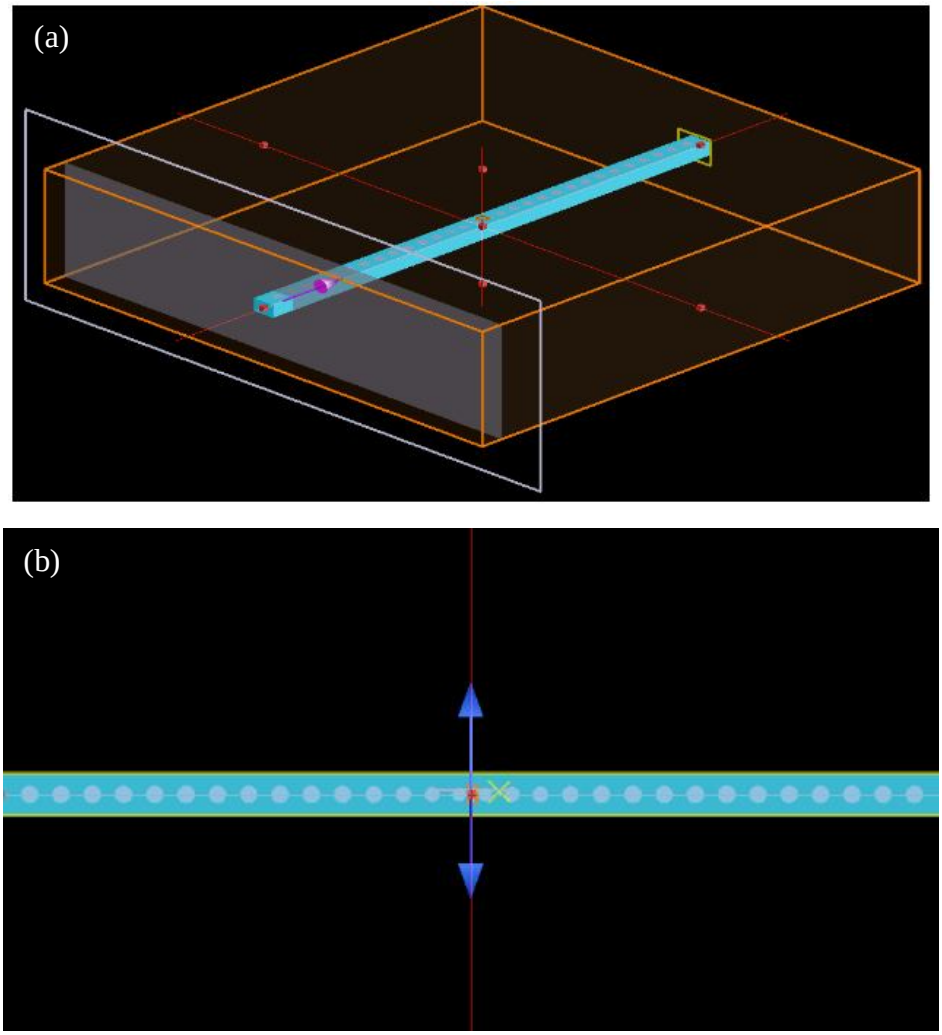

Figure 3.12 (a) A mode source injected at one end of a photonic nanobeam cavity inside a simulation region (outlined in orange). The direction of propagation is depicted by the pink arrow (b) An electric dipole located at an asymmetric region at the center of the nanobeam. The double sided blue arrow shows the direction of dipole polarization.

Summary

In this Chapter we briefly discussed two cutting-edge nanofabrication (FIB) and imaging (SEM) techniques, their drawbacks and ways to overcome them. A short description of fluorescence microscopy as a way of measuring nanofabricated samples is provided. The concept of Finite Difference Time Domain is briefly reviewed. We saw that FDTD is commercially used to make simulation software that in turn can be used to predict and verify the electromagnetic behaviour of a variety of customized nanostructures.

4. Integration of Metal Nanoparticle in Photonic Crystal Nanobeam Cavity

4.1. Introduction

This Chapter elaborates the design, fabrication and measurement details of hybrid photonic nanobeam cavities. As discussed in Section 2.5, hybrid plasmonic/photonic crystal integration strategies allow for enhanced emission from the photonic crystal cavities, while retaining reasonably large quality factors. In the previous works described in Chapter 2, the integration strategy consisted of multi-step fabrication techniques, for example, multistage electron beam lithography, deposition/lift-off [50] and etching, or alternatively combining electron beam lithography with dip-pen techniques. Here in our work, we showed that the entire process could also be accomplished in a single step, with FIB milling.

4.2. Design of the Hybrid Photonic Crystal Nanobeam / Silver Nanoparticle Structure

Photonic crystal nanobeam cavities have been theoretically proven to give quality factors of the order of a million while supporting a single resonance mode at 637 nm [24].We scaled those past designs to shift the cavity resonance to 600 nm. Figure 4.1 shows a schematic of the Si_3N_4 beam photonic cavity. The Bragg mirrors (as explained in Section 2.2.3) with a=225 nm and r=63 nm, were tapered down along four holes, symmetrically, around the center to a_1=184.5 nm and r_1=49.5 nm. A single silver ellipsoid nanoparticle (50 nm × 30 nm × 5 nm principle axes), with extinction peak (610 nm) close to the operating wavelength of the cavity, is placed at the center to show the configuration of our final assembly.

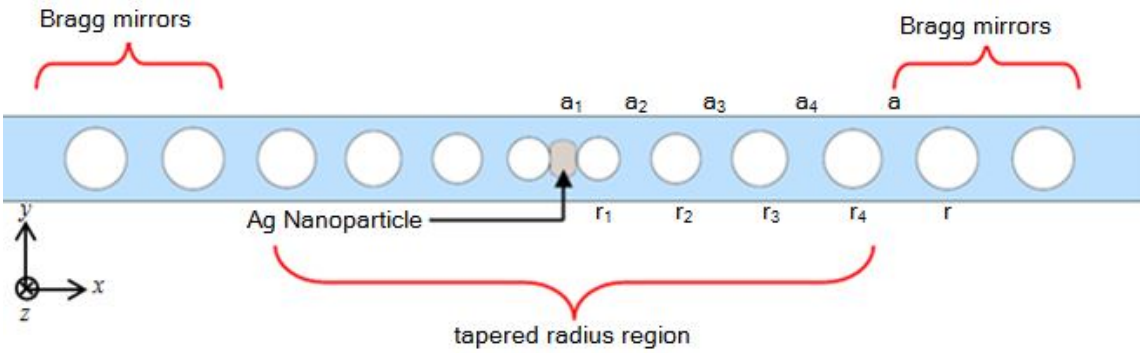

Figure 4.1 Schematic showing the arrangement of the hole radii and periodicities for a four-hole taper beam photonic cavity with the desired location of the metal nanoparticle.

A FDTD (Lumerical FDTD Solutions 7.5) simulation with PML boundary conditions was first performed on the cavity ($n \approx 2.00$) depicted in Figure 4.1 without the metal particle. To avoid artifacts from non-uniform auto-meshing, special graded mesh regions were created using manually controlled mesh override objects. These features offered by Lumerical FDTD Solutions 7.5 allow the user to specify the mesh step size for the simulation region in all directions. To allow uniformity in meshing, the mesh size in x, y and z directions were chosen, such that they were exact submultiples of the simulation volume in the respective directions. The structure was excited with a y-polarized electric dipole located slightly away from the center of the cavity (offset by 50 nm in x and y) to break the symmetry.

4.2.1. Quality Factor Calculation

Quality factors of cavities can be determined theoretically when the electromagnetic fields decay completely from the simulation in a time that can be simulated reasonably by FDTD. In this case, the quality factor is calculated from the Fourier transform of the field by finding the resonance frequencies of the signal and measuring the full width half maximum (FWHM) of the resonant peaks [51]. If f_r is the resonant frequency and Δf is the FWHM, the Q can be given by:

$$Q = \frac{f_r}{\Delta f} \tag{35}$$

In high quality photonic cavities, extremely long simulations are required to allow the field to completely decay to zero. Therefore, we calculate the quality instead from the slope of the envelope of the decaying signal (cavity ringdown, shown in Figure 4.2(a)) after allowing the simulation to run for 10 hours (corresponding to 1.5 ps in the simulation time) [52]. Q in this case is given by [47]:

$$Q = \frac{-2\pi f_r \log_{10} e}{2m} \tag{36}$$

where m is the slope of the log of the time signal envelope.

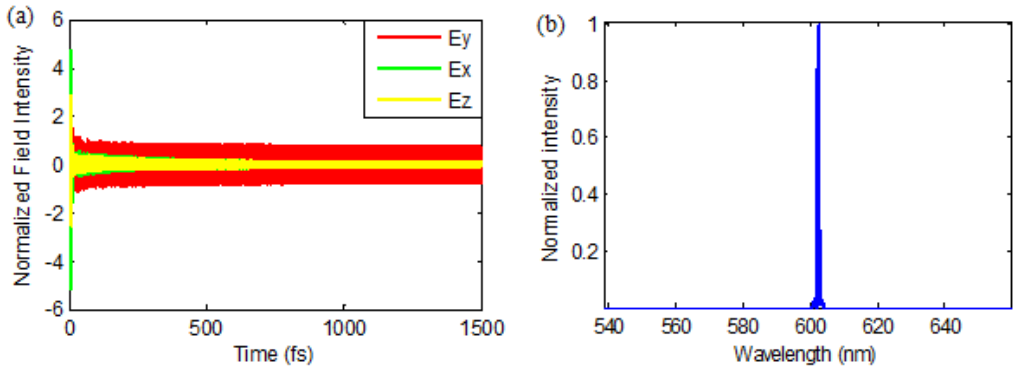

Figure 4.2 (a) Decaying electric fields with time. (b) Cavity resonance peak predicted at 602.24 nm.

The simulation results confirmed the presence of a single cavity resonance mode at 602.24 nm (shown in Figure 4.2(b)) for the bare cavity and the quality factor calculated using the above method was found to be ~65,000. The simulations were repeated with a cavity with the nanoparticle. Adding the nanoparticle (meshed with a 2 nm override mesh in all directions) resulted in a quality factor of ~1500 at a wavelength of 604.1 nm.

To investigate if a higher quality factor can be achieved with the same dimensions, the simulations were repeated with $n \approx 2.04$. This gave the resonant wavelengths as 610.2 and 611.96 nm and the quality factors as ~70,000 and ~1800 for cavities without and with the nanoparticles respectively.

Figure 4.3 shows the electric field intensity distribution 5 nm above the nanobeam (cutting through the middle of the nanoparticle) without and with the nanoparticle, using

a logarithmic (base 10) scale. The cavity with the nanoparticle has 4.5 times higher maximum local field intensity.

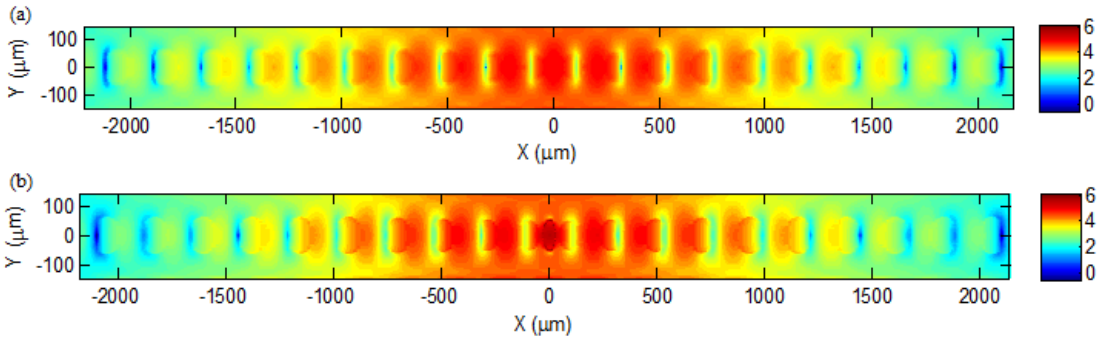

Figure 4.3 (a) Electric field distribution 5 nm above the nanobeam without the Ag nanoparticle at 610.2 nm (logscale). (b) Electric field distribution at the same height above the nanobeam with the Ag nanoparticle at 611.96 nm (logscale).

4.3. Nanoparticle Synthesis

Silver nanoparticles with a resonance around 600 nm were synthesized (nanoparticle synthesis procedure was conducted by Ghazal Hajisalem from our lab) using photoinduced colloidal assembly [53]. Spherical silver nanospheres were formed by the reaction between $NaBH_4$ and $AgNO_3$ in solution, in presence of trisodium citrate. The solution containing Ag spheres was mixed with a particle stabilizing agent (BSPP solution) and irradiated with a 60W white halogen light for 24 hours. This produced mostly ellipsoidal nanoparticles with an extinction peak at 610 nm. For longer exposure times that all the Ag particles evolve into nanoprisms with a peak in extinction at 670 nm, a small portion of them grow in to prisms much before that. For instance, some of the silver particles in the suspension that showed extinction at 610 nm were found to be prism shaped.

Figure 4.4(a) shows the scanning electron microscope (SEM) image of an ellipsoidal silver nanoparticle on Si_3N_4 membrane while 4.4(b) shows a fully formed silver nanoprism (on gold surface). Figure 4.4(c) depicts the extinction spectrum of the controlled-growth silver nanoparticles suspended in water, with a peak at a wavelength of 610 nm.

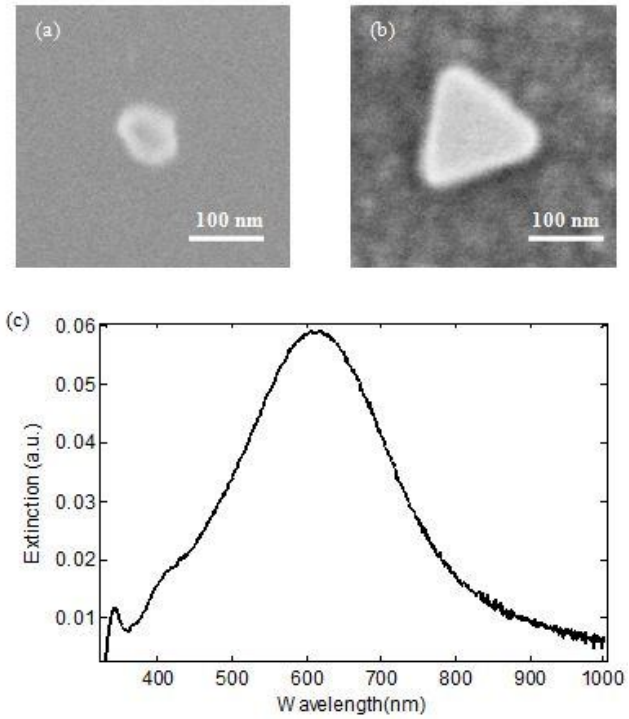

Figure 4.4 (a) Silver particle after 24 hours of irradiation showed on Si3N4 (b) silver prism after 72 hours of irradiation showed on gold (c) Extinction spectrum of aqueous suspension of silver nanoparticles synthesized in our lab, showing a peak at 610 nm.

4.4. Fabrication Procedure

The silver nanoparticle suspension was diluted by 20 times with deionized water and drop coated on a 9 × 9 grid comprising of 100 µm × 100 µm Si_3N_4 windows, each 200 nm thick (Ted Pella Inc.). The windows are held in place by a 200 µm thick Silicon support frame (Figure 4.5(a)). The solution was allowed to dry and the sample allowed to rest overnight in the evacuated FIB (Hitachi FB 2100) chamber. A secondary ion image detected the presence of silver particles on the surface of Si_3N_4 with a distribution of approximately 5-6 particles per 25 μm^2. To realize the structure without the nanoparticle, a spot was chosen such that any silver particles that lie in the region would be milled away by the beam. Particular care was taken to choose such a spot close to the edges of the Si_3N_4 windows. This is because, although Si_3N_4 is non-conductive, silicon is a semiconductor. Therefore, Si_3N_4 areas that are close to the support frame will have a better channel to allow the accumulating charges to escape. In other words, the less the

distance from the silicon frame, the less the charging effects, the better the quality of the cut.

Black and white bitmap images were used to indicate the size and shape of the structure to be cut (blackened areas are milled away) in this spot. The initial bitmap must be of maximum 2000×2000 pixels to completely fit the FIB work-station window. The magnification on the sample was then adjusted until the whole bitmap spanned the same exact area on the window (7.2 μm × 4.3 μm) as of the structure to be milled. Multiple overlapping bitmaps can be used to create one milling pattern (as was done in our case).

Gallium ions accelerated at 40 keV with a beam current of 10 pA and spot size of ~13.8 nm were at first used to drill the holes. One bitmap just consisting of the holes, shaped and spaced precisely, was used for this. Since the holes are the most sensitive part of a nanobeam cavity, they were drilled first so as to allow stronger support from the surrounding membrane, offering better-quality holes. The duration and the nature of how the drilling would progress were chosen with great care.

Hitachi FB 2100 offers the duration of a cut to be based on depth of the cut, a particular time length (say, 60 minutes, for example) or the number of passes (N) one scan of an ion beam of a particular time length (dwell time) may complete. Of these, the last option allows more granular control on the specifics of the cut. Dwell time can be defined as the length of time the beam will dwell on any given pixel of the bitmap. Alternating the direction of the scan in each pass makes the cuts uniform. For hole-drilling, a dwell time of 10 μs and N=400 produced the best results.

The adjacent 2 μm wide cavities were then rough-cut using another beam (spot size ~21.7 nm) with the same acceleration voltage but a beam current of 70 pA, a dwell time of 10 μs and with N=25. A second bitmap image overlapping the first was used to do this. Finally, the cavity edges were reshaped for 40 minutes with the same beam used to drill the holes, using the same dwell time and number of passes. Figure 4.4(b) shows a SEM image of one such cavity.

To realize a photonic cavity with the nanoparticle in it, the area was scanned to identify a single silver particle in isolation. Next it was necessary to make sure that the ellipsoidal particle was oriented perfectly transverse to the beam. The FIB window, in which milling patterns are superposed, is a direct feed from the sample chamber camera. The camera

angle was rotated until the view showed the particle to be perpendicularly aligned to the window. Then, the milling patterns were placed so that the center of the silver particle coincided (to within 10 nm) with the center of the nanobeam, in between its two smallest holes, and the major axis of the silver ellipsoid aligned with the *y*-axis of the beam, as shown in Figure 4.2(b) inset. After taking care that any other silver particles in the vicinity of the one selected would be milled away, the cavity was milled as before.

In total, 20 cavities were fabricated, 10 with and 10 without the nanoparticles. EDX (Bruker Quantax EDS) was performed later on the beam containing the silver particle. It confirmed the presence of silver nanoparticle after milling. Figure 4.5(b) (inset) shows the SEM image of a fabricated photonic crystal nanobeam cavity containing a nanoparticle.

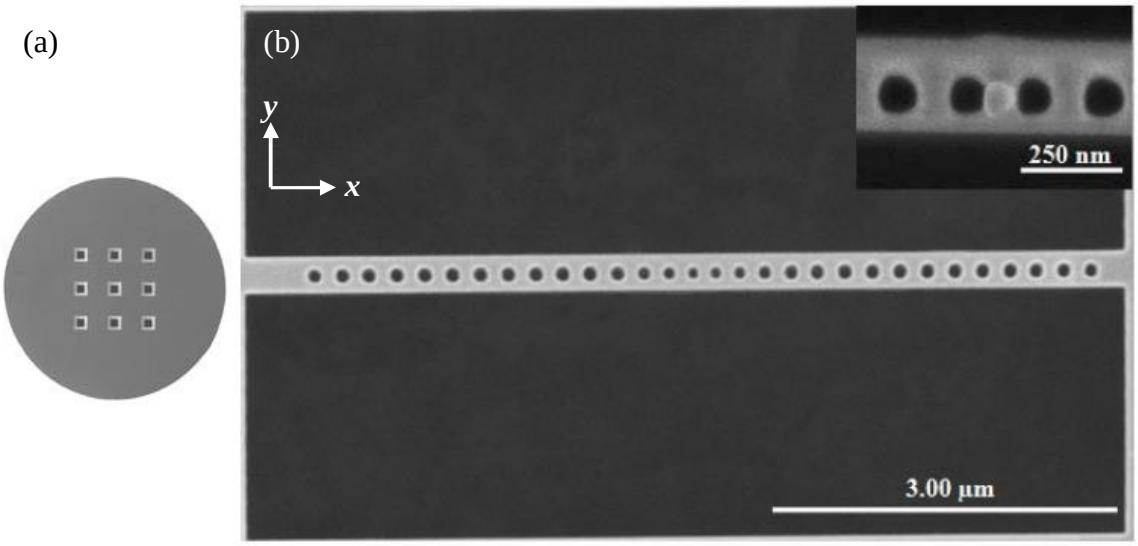

Figure 4.5 (a) SEM image of a 9 × 9 Si_3N_4 TEM grid from Ted Pella Inc. used for all fabrications (b)SEM image of a FIB fabricated photonic crystal nanobeam cavity on Si_3N_4. (Inset) Photonic crystal nanobeam cavity showing an ellipsoid nanoparticle at the centre.

4.5. EDX Measurements

EDX spectroscopy is prone to erroneous results if the detection area in the sample sits at a considerable lower height than the surrounding area, as in the case of a Si_3N_4 window on silicon frame. This is because the X-ray detector is situated at an angle to the horizontal sample stage. If the area of interest in the sample is located so deep that the edges surrounding it blocks a direct view from the detector, then the detector and the

electron beam are not necessarily looking at the same point on the sample. In such cases, it may display elements that although present in the sample, may be unexpected in the area the user is looking at. Moreover, in the absence of a direct path, the signal from the sample can be weak enough that mapping a particular expanse of it may take an extremely long time.

This issue can be addressed with a compromise of sample stage tilting. The stage can be tilted so that it is perfectly aligned with the detector but in this case, most of the sample surface will face away from the beam column and imaging the area of interest will become impossible. Therefore, a compromise between perfect alignment with the electron beam and alignment with the detector has to be made.

4.6. Imaging Nanobeam Cavities with SEM

SEM imaging the nanobeams offered a great deal of challenge in itself. Electrons, being much lighter than ions, are heavily affected by charging (as discussed in sections 3.2 and 3.3) in a mostly-nonconductive sample like a Si_3N_4 grid. Initially, chromium coating the sample was tried. Chromium is easy to remove with virtually no destructive effect on the rest of the sample. However, it was found to leave some residue behind which required cleaning of the sample. It was discovered that this could not be properly done without causing some damage to the fabricated nanostructures.

The second approach was to use thin wires of carbon paste connecting the silicon part of the grid directly to the Aluminum sample holder. As the sample was small and light enough to float on the tiniest drop of the paste, these wire attachments could only be done under a light microscope to prevent any damage. It was found that the air gaps between the sample and the stage (mostly due to long scratches on the holders) allowed the liquid paste to seep in below the grid. This resulted in the fabricated cavities being flooded and damaged (refer Figure 4.6 for an example). Moreover, incomplete drying of the paste, especially if some of it leaked under the sample, resulted in sample movement inside the SEM.

The third and final approach was to use little slices of carbon stickies. A slice of about 0.5 mm was cut and pasted across one side of the silicon frame so that it would not cover the windows. On the other hand, not covering enough surface area caused the sample to

stick out of the holder instead of lying flat on it. However, when correctly done, this approach helped solve a lot of imaging issues.

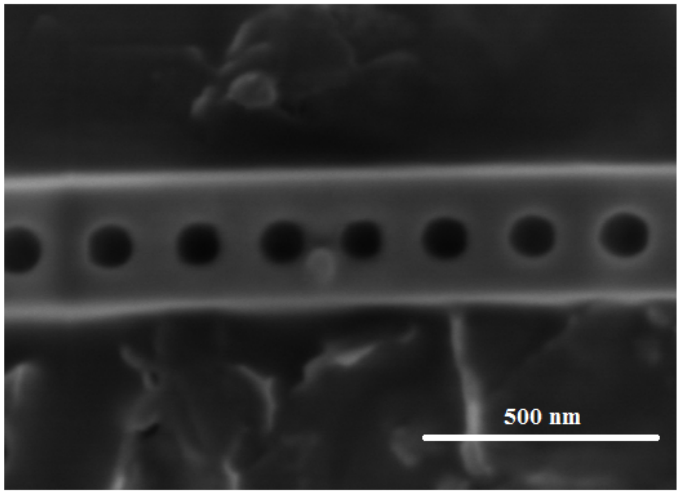

Figure 4.6 Photonic nanobeam cavity damaged by excessive carbon paste leakage underneath.

4.7. Fluorescence Measurements

The fabricated beam cavities were characterized using fluorescence microscopy. A 514 nm Argon ion laser was allowed to stabilize to a power output of 230 mW in a constant current mode (20 A). In some of the earliest experiments, the laser power used was high enough to melt the fabricated nanobeams. The intensity was therefore gradually reduced using Neutral Density (ND) filters, until the beams held well, even after repeated laser exposures. Care was taken to see that the laser intensity did not fall so low so as not to record a readable signal on the spectrograph.

After many adjustments, both types of cavities were excited with ~875μW of power from the laser (Si_3N_4 gives off a broad fluorescence spectrum between 580 nm and 680 nm). Such amount of power caused very negligible heating of the beam or that of the nanoparticle. The focal point of heating was small enough to allow the heat to be dissipated to the surroundings quickly.

Obtaining the microscopy results required focusing the laser beam on the center of the cavity, as shown in Figure 4.5. Focusing away from the center gave negligible fluorescence. The laser was focused to the spot that gave the largest intensity in each case. Fluorescence from Si_3N_4, emitted out of the plane from the membrane, was

collected using a 100× /0.9 NA microscope objective for 5 accumulations, each with 10 seconds exposure time (to increase the SNR). It was measured with a 0.25 m Czerney-Turner spectrometer, containing an 1800 lines/mm grating, and using a Peltier cooled CCD. The gratings help diffract the incoming light into its components. The direction of the component beams depend on the gratings spacing and the wavelength of light.

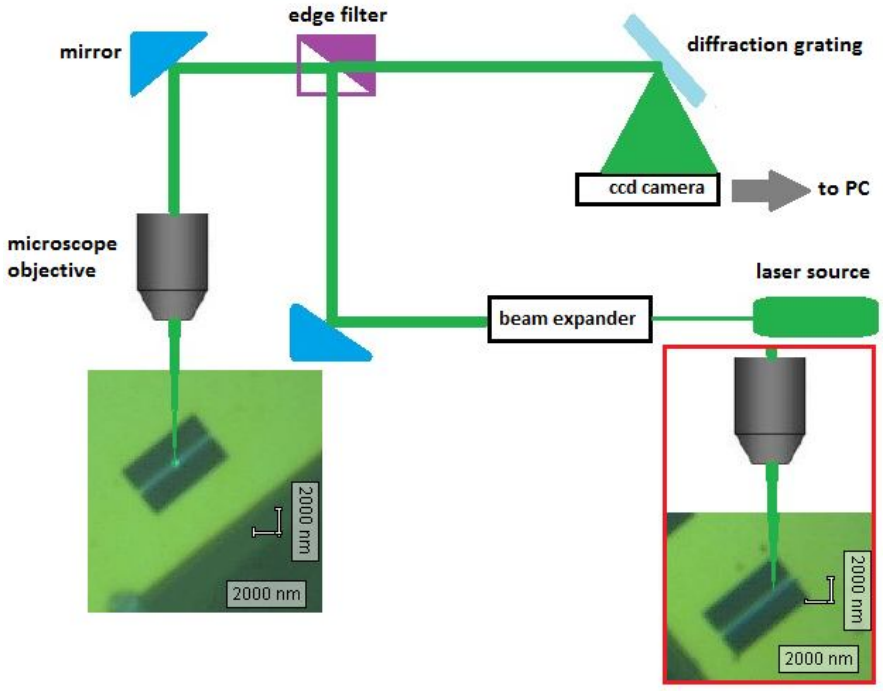

Figure 4.7 Schematic showing the fluorescence microscopy setup and the actual laser spot focused at the center of one of the characterized nanobeams.(Inset) Schematic of the laser spot focused off-center on the nanobeam.

4.7.1. Measurement Results

Figures 4.8(a) and 4.8(b) show the fluorescence emission for cavities without the Ag nanoparticle. In Figure 4.8(a), a scan over a range of 580 nm to 660 nm shows a single sharp peak for the bare cavity at 590 nm over a broad background. In Figure 4.8(b), a Lorentzian curve fit [54] on the peak data points shows an FWHM ($\Delta\lambda$) of 0.1 nm. Unfortunately, our spectrometer resolution was 0.07 nm, so that the quality factor of the highest quality cavities, with a linewidth of 0.1 nm could not be determined accurately. We used Lorentzian fitting and deconvolution [55] to estimate the quality factor to be 20,000 ± 3,000, which is below the value of 55,000 that has been found in other experiments [24].

Figures 4.8(c) and 4.8(d) show the fluorescence emission for cavities with the Ag nanoparticle. Figure 4.8(c) shows a single peak at 597.5 nm with 5 times higher intensity counts than Figure 4.8(a). The enhancement factor was determined by taking ratio of the peak heights and subtracting the background, for the same excitation intensity. The background was typically the same in both cases (with and without the particle), and the peak height and the background both scaled linearly with the excitation laser power (in the low power excitation regime). Fitting Figure 4.8(d) to a Lorentzian, the peak data points are found to show a $\Delta\lambda$ of 0.5 nm, so that the quality factor is estimated to be 1200.

In total, 10 cavities without the nanoparticles were fabricated and their reproducibility tested, as shown in Figure 4.8(e) and 4.8(f). To ensure reproducibility, the cavities were characterized on multiple days. Figure 4.8(f) shows that the cavities without Ag nanoparticles had approximately the same peak height for all 10 cavities fabricated (blue squares).

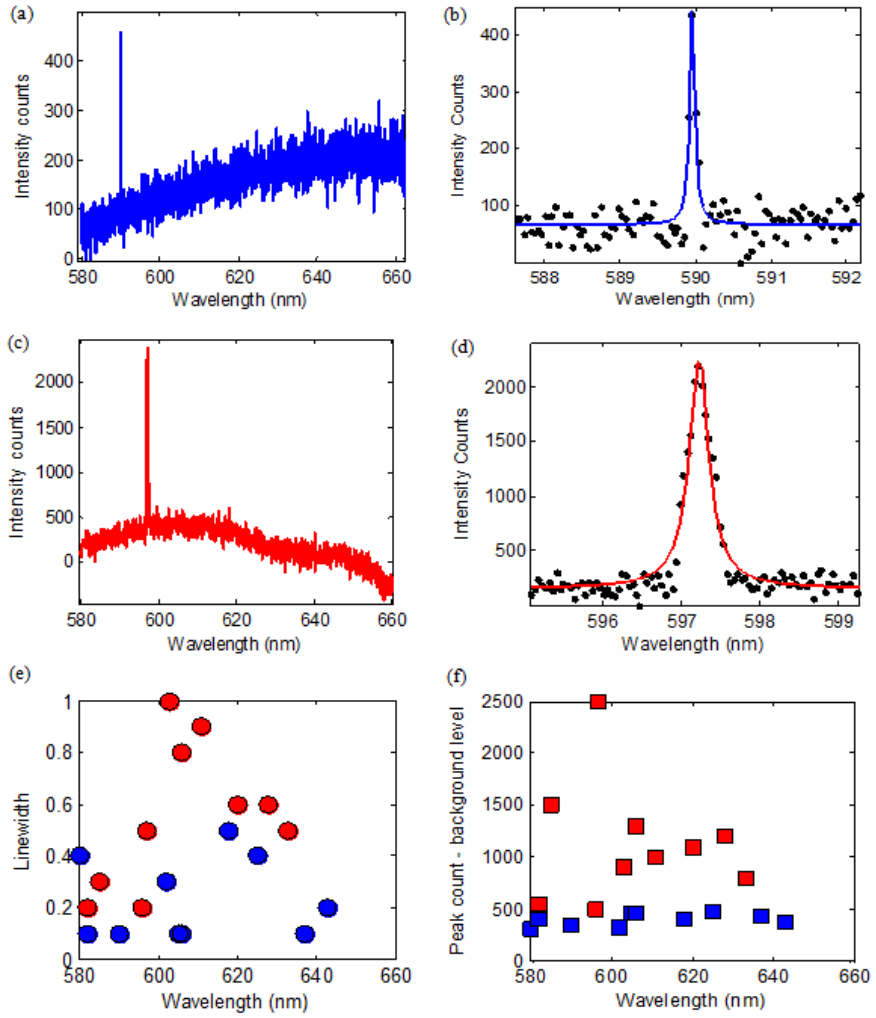

Figure 4.8 (a) Fluorescence emission spectrum and (b) Lorentzian fit on cavities without nanoparticle (blue). (c) Fluorescence emission spectrum and (d) Lorentzian fit on cavities with nanoparticle (red). Data points are shown in black. (e) Linewidth and wavelength of the fabricated cavities without (blue) and with (red) the nanoparticle. (f) Net intensity counts (peak count-average background count) achieved from the cavities at various resonance wavelengths.

For the cavities with the nanoparticles, the wider FWHM is expected to arise from a combination of enhanced radiative coupling and increased losses due to the presence of the Ag nanoparticle. Similarly, the enhanced fluorescence intensity is attributable to the enhanced radiative coupling, as well as the enhanced local density of photonic states allowed by the metal nanoparticle. Separation of the radiative contributions from the

local field effects requires further studies, for example, by noting relative changes in emission lifetime and emission intensity.

4.8. Measurements on a Single Cavity with and without the Ag Nanoparticle

It should be noted that it is not strictly valid to compare different cavities with one another, even though they were fabricated with nominally the same procedure. Therefore, we took the cavity with the highest enhancement and etched away the Ag nanoparticle with 7M nitric acid for 5 min (typical etch rate of 400 nm/min at 20ºC) [56, 57]. Figure 4.9 shows a blue-shift of 4 nm and reduction in the peak height (by 5 times) when removing the nanoparticle. This result is consistent with both the simulations (in terms of the wavelength shift) and the above measurements on multiple cavities (in terms of the enhancement factor).

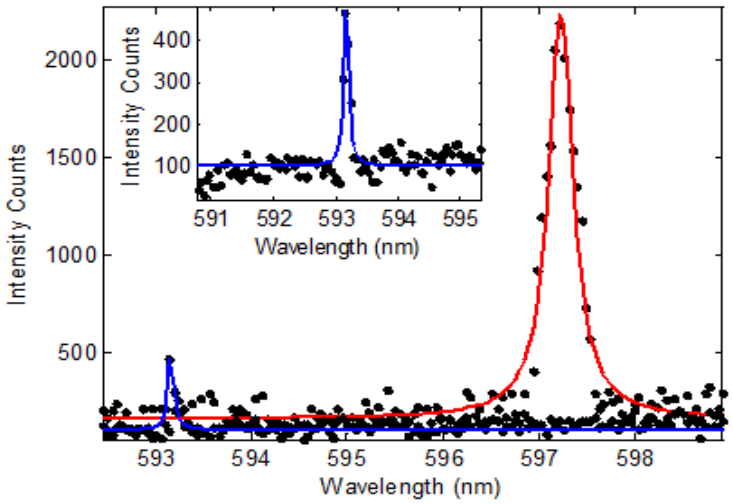

Figure 4.9 Measurements taken from the same cavity before (red) and after (blue) the removal of the nanoparticle. (Inset) Zoom in on the blue curve showing the decreased intensity counts and linewidth compared to the red.

4.9. Discussion

There have not been many well documented cases as to what may be the best quality factor that a hybrid nanocavity can offer for a SPS to perform optimally. Various studies have shown substantial single photon emissions from dielectric microcavity-coupled QDs or NV centers, with quality factors of the microcavities ranging from as low as 300 [58] to as high as 50,000 [13]. In all of them, compromises were made either on extraction

efficiencies, coupling efficiencies or on frequency of emission. Moreover, the cavities were typically not designed to operate in visible optical frequencies. Therefore, a quantitative way to compare our achieved quality factor in terms of performance in a SPS was not found.

4.10. Summary

A one-step fabrication process for the integration of size-controlled resonant Ag nanoparticles within a suspended Si_3N_4 nanobeam photonic crystal cavity is demonstrated in this Chapter. The steps followed in fabrication and imaging the nanostructures have been detailed. The experimental results have also been discussed in details. It was observed that, the emission wavelength in the experiments was close to the designed value. The quality factor of the cavity with the Ag nanoparticle was estimated at 1200 with enhanced radiative coupling, which suggests that these measurements are promising for future single photon emission studies incorporating quantum dots or NV centers [36, 59].

5. Analysis of Hybrid Plasmonic-Photonic Crystal Structures using Perturbation Theory

5.1. Introduction

The photonic nanobeam cavities that are described in Section 4 typically support a resonant mode at ~ 600 nm and have a quality factor of ~55,000 (theoretically) for n=2.0. Inserting a small silver nanoparticle at the center of the nanobeam has been found to lower the resonant frequency as well as the quality factor of the cavity, the latter by a factor of 20 [60]. This Chapter is devoted to explaining how the same can be achieved using perturbation theory. An example calculation is shown, agreeing to within 5% with comprehensive finite-difference time-domain simulations, but taking an order of magnitude less time.

5.2. Perturbation Theory Application to a Hybrid Plasmonic-Photonic Structure

While the word 'perturbation' is usually associated with an approximate formulation [61-64], it is stressed that the perturbation theory presented here (following past microwave approaches [42]) is a nearly exact formulation except for the adhoc treatment of the scattering losses. It must be considered that the expression for the new quality factor described in Section 2.6.1, only accounts for the absorption losses due to the perturbing particle [42]. This is because, the cavity in the original theory is assumed to consist of perfectly conducting walls [65].

5.2.1. Introduction of Scattering Losses

In order to calculate the contribution from scattering losses of the added particle in addition to the absortion losses, we separate the absorption and scattering times using absorption and scattering cross sections of the particle, represented by C_{abs} and C_{scat} respectively. τ_{scat} can be calculated from the following expression [66]:

$$\tau_{scat} = \tau_{abs}\left(\frac{C_{abs}}{C_{scat}}\right) \tag{37}$$

where τ_{abs} is the absorption time given by $\frac{Q_a'}{\omega}$.

The modified quality factor accounting for both scattering and absorption, Q', is now given by the expression $Q' = \omega\tau'$ where τ' can be obtained as:

$$\frac{1}{\tau'} = \frac{1}{\tau_{scat}} + \frac{1}{\tau_{abs}} \tag{38}$$

Hence, provided that the fields of the resonant cavity before the perturbation and the fields inside the perturbing sample after the perturbation are known, the shift in the frequency of the cavity and its quality factor can be calculated readily. For solving the problems of resonant hybrid photonic crystal cavities theoretically, it has been showed in a later Section that, this property of perturbation theory can save simulation time and memory, while predicting accurate changes in resonant frequencies and quality factors.

5.2.2. Applying Perturbation Theory to a Nanobeam Cavity with Ag Nanoparticle

The approach to the problem is shown in Figure 5.1. The 3D schematic of Figure 5.1(a) has been broken down into 2D cavities shown before (Figure 5.1(b)) and after (Figure 5.1(c)) perturbation. After exciting the 6800×300×200 nm^3 nanobeam with a mode source centered at the resonant frequency of the cavity (shown in Figure 5.1(a)), we obtain the unperturbed electric and magnetic field values (E_1 and H_1) of the cavity over the entire FDTD simulation region (6800×4300×1800 nm^3) that represents the cavity volume (Figure 5.1(b)). Next, a silver nanoparticle is placed at the center of the nanobeam and the perturbed cavity fields (E' and H') are obtained from the vicinity of the nanoparticle (white shaded region in Figure 5.1(c)) while it still rests on the beam. Following discussions in section 2.6.1, the shaded region extends to 150 nm in all directions from the particle. This distance was chosen by inspection of the simulation domain over which the field from the nanoparticle has decayed to below 10^{-6} times its maximum value.The subsequent frequency shifts and reduced quality factors can now be calculated from the equations described in Section 2.6.1.

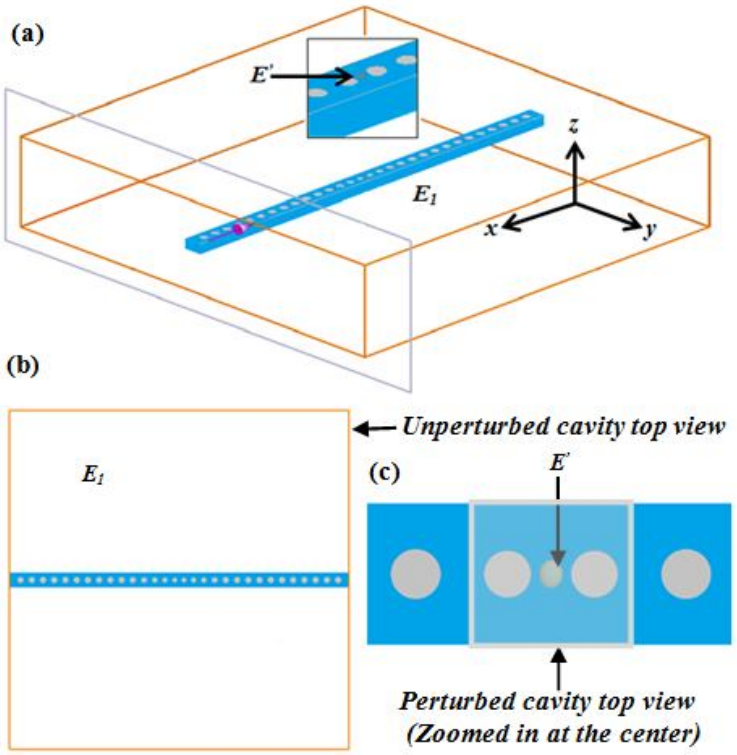

Figure 5.1 (a) 3D schematic showing the photonic crystal nanobeam with a nanoparticle inside the simulation region. The pink arrow shows the direction of the propagation of the mode. The inset is a close-up on the nanoparticle at the center. (b) Top view of the nanobeam in the simulation region, forming an unperturbed cavity. (c) Zoom-in to the center of the nanobeam after the introduction of the nanoparticle. The shaded area shows the perturbed region considered.

To have a resonant enhancement, we tuned the plasmonic resonance of the silver nanoparticle on silicon nitride to that of the cavity. We used Johnson and Christy Ag database which offers lower losses, to conduct the simulations [67]. It was found that a particle of size 60×52×10 nm^3 produces an extinction peak at ~600 nm as shown in Figure 5.2(a), when simulated on a silicon nitride substrate. Figure 5.2(b) shows a cross Section of the particle on silicon nitride indicating non-uniformity of fields inside the particle due to the effect of the substrate.

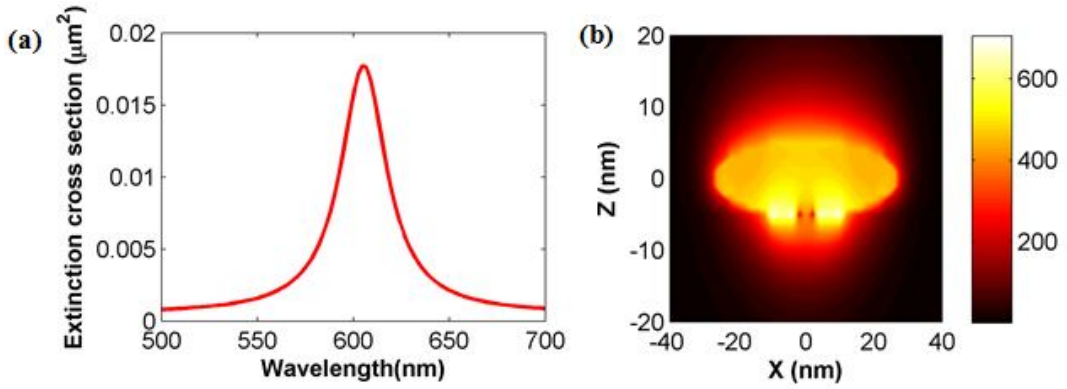

Figure 5.2 (a) The scattering cross Section of a 60×52×10 nm^3 silver nanoparticle on a 200 nm thick blank Si_3N_4 substrate. (b) A transverse cross Section through the nanoparticle showing the electric field distribution inside (linear scale).

5.3. Theory Results and Verification

5.3.1. Calculation with a Photonic Nanobeam Cavity

Since , E_1, H_1 and Q_1 have to be known in order to implement our theory, we ran FDTD simulations (using Lumerical FDTD Solutions 7.5) on the bare nanobeam cavity to collect the fields, while noting the corresponding resonant frequency and quality factor. The other two known quantities, E' and H' were similarly collected from FDTD simulations on the nanoparticle.

To account for the effects of the cavity whose presence causes a huge concentration of field intensity in the substrate, the fields (E' and H') obtained from within the 150 nm radius of the nanoparticle, in the nanoparticle simulations were normalized to the same base intensity i.e. at the points in the Si_3N_4 substrate where they coincided (from the cavity and the nanoparticle simulations), we considered the field values in Si_3N_4 from the cavity simulations rather than the field values in Si_3N_4, given by the nanoparticle simulation.

We initially attempted a perturbation approach on our test case that simply assumed the standard dipole polarizability of the ellipsoid [31] in the cavity field. In this case, the frequency shift and quality factor were found to be 0.457 THz and 808.6 which was not in good agreement with the FDTD results (2.32 THz and 679.08).

Applying the modified perturbation theory next, E_2 and H_2 were obtained using Eqs. (19) and (20). D_1 and B_1 were calculated from Eqs. (17) and (18) while D_2 and B_2 from Eqs. (21) and (22). Similar to our simulations, we used Johnson and Christy database to determine the ε_2 of the particle, which at the resonance wavelength of 600 nm, is $-16.0859 + 0.4429\text{i}$. μ_2 was assumed to be 1.The calculated values were then substituted in Eq. (31) to obtain the complex resonance shift. As shown in Eq. (31), only the real component of this expression can give the frequency shift, which was calculated to be 0.32 THz. The quality factor due to absorption, $Q_a^{'}$, from Eq. (35) was calculated to be 2469.4. C_{abs} and C_{scat} were next obtained from nanoparticle simulations by subtracting the incident source field from the scattered field outside the source region. Using Eq. (38), Q_{scat} therefore calculated from the expression $Q_{scat} = \omega\tau_{scat}$ was found to be 3431.3. Finally, following Eq. (39), $Q^{'}$ was calculated to be 1436.

To verify the results, the nanoparticle was meshed with a mesh step size 5 times smaller than the cavity in x and y directions and 10 times smaller in z direction and FDTD simulations were conducted. The simulations showed a frequency shift of 0.36 THz and a quality factor of 1501.9, which agrees within 5% of the results predicted by our perturbation theory. The sources of error may involve finite domain mesh size when simulating the field change around the particle, numerical errors and the ad hoc method of calculating the quality factor.

In terms of calculation time, the bare cavity simulations took about 3.3 hours to run while the nanoparticle simulation took about 0.7 hours. A full cavity simulation with the nanoparticle took 48 hours to run. This indicates that our theory was able to cut down the total computation time by a factor of 12.

To show that a full recalculation was not necessary if the nanoparticle was changed, we replaced the ellipsoidal particle with a rectangular silver nanorod of dimensions $60\times100\times10$ nm^3, applied perturbation theory and verified the results using FDTD. Our theory predicted a frequency shift of 1.39 THz and a quality factor of 1270.17, as compared to FDTD which calculated a frequency shift of 1.42 THz and a quality factor of 1327.67.

5.3.2. Calculation with a Waveguide Cavity

To test the effect of our theory on other hybrid structures, we replaced the nanobeam cavity with a reduced hybrid cavity using PEC walls as mirrors instead of the photonic crystal holes. Calculations were repeated using the ellipsoidal particle as the source of perturbation and a mesh step size of 1 nm in all directions to achieve the best possible convergence in a reasonable simulation time.

To set up the reduced cavity, the intended resonant wavelength ($\lambda_0 \approx 600$ nm) is at first used to calculate the wavelength of the mode (λ_{wg}), propagating through a given block of silicon nitride ($n_{eff} = 1.569$). λ_{wg} can thus be expressed as:

$$\lambda_{wg} = \frac{\lambda_0}{n_{eff}} \tag{39}$$

Setting $x = \frac{1}{2}\lambda_{wg}$, $y = 300$ nm and $z = 200$ nm of the silicon nitride block, we allowed perfectly conducting boundaries in x direction (direction of propagation of the mode) and PML boundaries in y and z directions. A small amount of loss was introduced to the dielectric in the above lossless system to bring down the quality factor to a value comparable to that of the photonic nanobeam cavity. Simulations were conducted with and without the nanoparticle to obtain the fields as before.

Perturbation theory when applied to this cavity produced a frequency shift of 2.29 THz and a quality factor of 1157.9. These results were supported to within 5% by the FDTD simulations showing a frequency shift of 2.23 THz and a quality factor of 1208.86.

5.3.3. Discussion

From the sections 5.3.1 and 5.3.2, we can conclude that, both the cases of changing nanoparticle and changing cavity showed good agreement between the numerical simulation and the perturbation method. It was also observed that with a larger mesh size of 2 nm in the z-direction, the difference between the FDTD and perturbation method was 11 %. This can be improved to 4.4% at the expense of increased simulation time using a finer grid of 1 nm, which is found to be a good compromise between reasonable computation times and accuracy. It is possible to consider extending this approach to

whispering gallery mode cavities and multiple metal nanoparticles, but so far, such a diversity of calculations has not been attempted.

Figure 5.3 shows the cavity resonant frequencies and quality factors for the photonic crystal nanobeam cavities with and without the nanoparticle in terms of wavelengths.

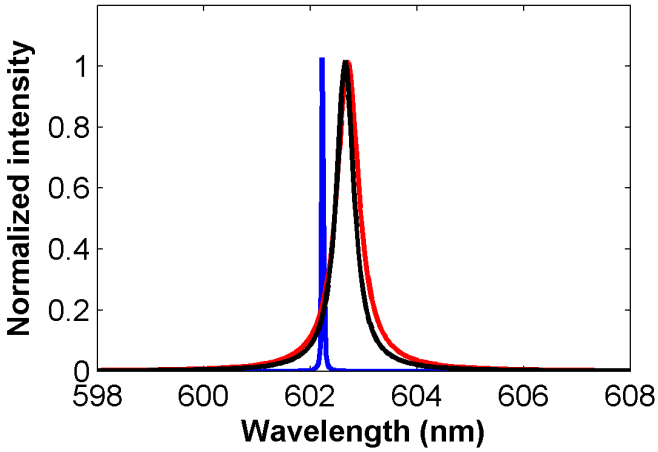

Figure 5.3 The shift in the photonic nanobeam cavity frequency and the change in the quality factor with and without (blue) the addition of the nanoparticle from FDTD simulations (black) and perturbation theory (red).

5.4. FDTD Solvers on Supercomputer Clusters

The cavity simulations tended to need large computation power to produce accurate results. On local laboratory computers (using twelve processor cores), they usually consumed up to two-three days to complete one run. Therefore, simulations were carried out using High Performance Computing (HPC) facilities offered by Compute Canada [68]. Under this facility, we had access to SHARCNET, a group of 64-bit high performance Opteron and Xeon clusters with around 20,000 CPUs, along with a group of storage units, based in Ontario, and WestGrid, its equivalent in Canadian west coast. Simulation jobs were uploaded to the FDTD running clusters (Orca for SHARCNET, Orcinus for WestGrid), set up to run parallel on twenty processors, with a maximum runtime of 80 hours. Finished jobs were downloaded and saved on local computers.

5.5. Summary

In this work, we calculated the resonance frequency shifts and quality factors of hybrid plasmonic nanoparticle/photonic crystal cavities after the introduction of the metal

nanoparticle using perturbation theory. For an example calculation, the results were tested against comprehensive FDTD, showing agreement to within 5%. The technique based on a hybrid approach is found to be particularly insightful for analyzing the global and local field contributions in hybrid photonic crystal cavities, allowing for an order of magnitude speed up in the calculations. The results are promising for future applications especially involving large geometries, resulting in faster design process [69].

6. Conclusion and Future Work

Photonic crystal nanobeam cavities, with their high quality factors and uncomplicated fabrication techniques, can be used to realize hybrid photonic-plasmonic devices. Such devices are excellent candidates for single photon generation, which is the key requirement for quantum cryptography and quantum information processing.

In this work, we demonstrated how FIB milling can be successfully used for one step fabrication of hybrid nanobeam cavities. Experiments repeated with multiple such cavities exhibited reasonably good quality factors (~1200) while showing up to five times local field enhancement as compared to bare nanobeam cavities. The design, fabrication and measurement details of these cavities have been discussed in Chapter 4.

It was found that theoretically simulating these cavities using FDTD multiple times is cumbersome. Changing the shape of the cavity or changing the plasmonic particle requires a repeat computation and there consumes a significant amount of computation time and memory. Chapter 5 of this work therefore focusses on applying Perturbation theory to calculate the resonant peaks and quality factors of hybrid cavities. This results in a 12 times faster design process while preventing repeat computations of the entire structure, if either the cavity or the nanoparticle is changed.

Our theoretical and experimental results have been published in:

- Ishita Mukherjee, Ghazal Hajisalem and Reuven Gordon, “One step Integration of metal nanoparticles in photonic crystal nanobeam cavity,” Optics Express, 19, 22462-22469 (2011).
- Ishita Mukherjee, Ghazal Hajisalem and Reuven Gordon, “Photonic crystal nanobeam cavities for single step metal nanoparticles integration”, 11th IEEE Conference on Nanotechnology, 969-972 (2011).
- Ishita Mukherjee and Reuven Gordon, “Analysis of hybrid plasmonic-photonic crystal structures using perturbation theory”, Optics Express, 20, 16992-17000 (2012).

6.1. Future Work

For the next step, the hybrid cavities can be integrated with quantum dots emitting at the same wavelength as the resonance of the cavities. To realize such integration, the quantum dot has to be bound to the nanoparticle at the point of its greatest field concentration [70]. One way to do this is to use functionalized quantum dots that have special affinity for a particular metal [71]. However, it has to be made sure that the solution liquid for quantum dots does not affect the photonic-plasmonic assembly in any way [72]. Different types and shapes of metal nanoparticles can be tested to achieve the best possible enhancement while reducing losses [73, 74].

It may be possible to increase the observable intensity enhancement in the fabricated cavities by using a higher resolution spectrometer with a longer focal length. Better resolution will also reduce spectrometer convolution and allow a more accurate calculation of measured quality factors, reducing the predicted error margins.

Bibliography

1. Walther, H., et al., *Cavity quantum electrodynamics.* Reports on Progress in Physics, 2006. **69**(5): p. 1325-1382.
2. Gonzalez-Tudela, A., et al., *Entanglement of Two Qubits Mediated by One-Dimensional Plasmonic Waveguides.* Physical Review Letters, 2011. **106**(2).
3. Badolato, A., et al., *Deterministic Coupling of Single Quantum Dots to Single Nanocavity Modes.* Science, 2005. **308**(5725): p. 1158–1161.
4. Englund, D., et al., *Controlling the Spontaneous Emission Rate of Single Quantum Dots in a Two-Dimensional Photonic Crystal.* Physical Review Letters, 2005. **95**(1).
5. Lodahl, P., et al., *Controlling the dynamics of spontaneous emission from quantum dots by photonic crystals.* Nature, 2004. **430**: p. 654-675.
6. Ryu, H.-Y., M. Notomi, and Y.-H. Lee, *High-quality-factor and small-mode-volume hexapole modes in photonic-crystal-slab nanocavities.* Applied Physics Letters, 2003. **83**(21): p. 4294.
7. Maier, S.A., *Effective Mode Volume of Nanoscale Plasmon Cavities.* Optical and Quantum Electronics, 2006. **38**(1-3): p. 257-267.
8. Ozbay, E., *Plasmonics: merging photonics and electronics at nanoscale dimensions.* Science, 2006. **311**: p. 189–193.
9. Schuller, J.A., et al., *Plasmonics for extreme light concentration and manipulation.* Nature Materials, 2010. **9**: p. 193–204.
10. Grillet, C., et al., *Nanowire coupling to photonic crystal nanocavities for single photon sources.* Optics Express, 2007. **15**: p. 1267–1276.
11. Falk, A.L., et al., *"Near-field electrical detection of optical plasmons and single-plasmon sources.* Nature Physics, 2009. **5**: p. 475–479.
12. Purcell, E.M., *Spontaneous emission probabilities at radio frequencies.* Physical Review, 1946. **69**: p. 681.
13. Strauf, S., et al., *High-frequency single-photon source with polarization control.* Nature Photonics, 2007. **1**(12): p. 704-708.
14. Pelton, M., et al., *Efficient Source of Single Photons: A Single Quantum Dot in a Micropost Microcavity.* Physical Review Letters, 2002. **89**(23).
15. Painter, O., et al., *Two-Dimensional Photonic Band-Gap Defect Mode Laser.* Science, 1999. **284**: p. 1819-1821.
16. Vahala, K., *Optical Microcavities.* Nature, 2003. **424**: p. 839-846.
17. Gérard, J.M., et al., *Enhanced Spontaneous Emission by Quantum Boxes in a Monolithic Optical Microcavity.* Physical Review Letters, 1998. **81**: p. 1110-1113.
18. Armani, D., et al., *Ultra-high-Q toroid microcavity on a chip.* Nature, 2003. **421**: p. 925-928.
19. Foresi, J., et al., *Photonic-bandgap microcavities in optical waveguides.* Nature, 1997. **390**: p. 143-145.
20. Tandaechanurat, A., et al., *Increase of Q-factor in photonic crystal H1-defect nanocavities after closing of photonic bandgap with optimum slab thickness.* Optics Express, 2008. **16**: p. 448-455.

21. Barth, M., et al., *Modification of visible spontaneous emission with silicon nitride photonic crystal nanocavities.* Optics Express, 2007. **15**: p. 17231–17240.
22. Barth, M., et al., *Emission properties of high-Q silicon nitride photonic crystal heterostructure cavities.* Applied Physics Letters, 2008. **93**(2): p. 021112.
23. Khan, M., et al., *Fabrication and characterization of high-quality-factor silicon nitride nanobeam cavities.* Optics Letters, 2011. **36**: p. 421–423.
24. Lončar, M. and M. McCutcheon, *Design of a silicon nitride photonic crystal nanocavity with a Quality factor of one million for coupling to a diamond nanocrystal.* Optics Express, 2008. **16**: p. 19136–19145.
25. Purcell, E., H. Torrey, and R. Pound, *Resonance Absorption by Nuclear Magnetic Moments in a Solid.* Physical Review, 1946. **69**(1-2): p. 37-38.
26. Novotny, L. and B. Hecht, *Principles of Nano-optics*. 2006, New York: Cambridge University Press.
27. Maier, S.A., *Plasmonics: Fundamentals and Applications*. 2007, New York: Springer Science+Business Media LLC.
28. Maier, S.A. and H.A. Atwater, *Plasmonics: Localization and guiding of electromagnetic energy in metal/dielectric structures.* Journal of Applied Physics, 2005. **98**(1): p. 011101.
29. Maier, S.A., *Plasmonics: metal nanostructures for subwavelength photonic devices.* IEEE Journal of Selected TOpics in Quantum Electronics, 2006. **12**: p. 1214–1220.
30. Andreani, L.C. and G. Panzarini, *Strong-coupling regime for quantum boxes in pillar microcavities: Theory.* Physical Review B, 1999. **60**(19): p. 13276-13279.
31. Bohren, C.F. and D.R. Huffman, *Absorption and Scattering of Light by Small Particles* 1983, New York: John Wiley & Sons, Inc.
32. Jackson, J.D., *Classical Electrodynamics*. 1999, New Jersey: John Wiley and Sons, Inc.
33. Min, B., et al., *High-Q surface-plasmon-polariton whispering-gallery microcavity.* Nature, 2009. **457**(7228): p. 455-8.
34. De Angelis, F., et al., *A hybrid plasmonic-photonic nanodevice for label-free detection of a few molecules.* Nano Lett., 2008. **8**: p. 2321–2327.
35. Barth, M., et al., *Nanoassembled plasmonic-photonic hybrid cavity for tailored light-matter coupling.* Nano Lett, 2010. **10**(3): p. 891-5.
36. Barclay, P.E., et al., *Hybrid photonic crystal cavity and waveguide for coupling to diamond NV-centers.* Opt. Express, 2009. **17**: p. 9588–9601.
37. Maksymov, I.S., *Optical switching and logic gates with hybrid plasmonic-photonic crystal nanobeam cavities.* Phys. Lett. A, 2011. **375**: p. 918–921.
38. Shields, A.J., *Semiconductor quantum light sources.* Nat. Photonics, 2007. **1**: p. 215-223.
39. Curto, A.G., et al., *Unidirectional emission of a quantum dot coupled to a nanoantenna.* Science, 2010. **329**(5994): p. 930-3.
40. Kondylis, G.D., et al., *A memory efficient formulation of the finite difference time domain method for the solution of Maxwell's equations.* IEEE Transactions on Microwave Theory and Techniques, 2001. **49**(7): p. 1310–1320.

41. Liu, Y., et al., *A memory efficient strategy for FDTD implementation applied to photonic crystal problems.* Progress in Electromagnetic Research, 2007. **3**: p. 374–378.
42. Waldron, R.A., *Theory of Waveguides and Cavities*. 1967, London: Maclaren & Sons.
43. Lalouat, L., et al., *Near-field interactions between a subwavelength tip and a small-volume photonic-crystal nanocavity.* Physical Review B, 2007. **76**(4).
44. Goldstein, J.I. and Y. Harvey, *Practical scanning electron microscopy*. 1975, New York: Plenum Press.
45. Yee, K.S., *Numerical Solution of Initial Boundary Value Problems Involving Maxwell's Equations in Isotropic Media.* IEEE Transactions on Antennas and Propagation, 1966. **14**(3): p. 302-307.
46. Yu, W. and R. Mittra, *A Conformal Finite Difference Time Domain Technique for Modeling Curved Dielectric Surfaces.* IEEE Microwave and Wireless Components Letters, 2001. **11**(1): p. 25-27.
47. Lumerical. *http://www.lumerical.com/*.
48. Mur, G., *Absorbing Boundary Conditions for the Finite-Difference Approximation of the Time-Domain Electromagnetic-Field Equations.* IEEE Transactions on Electromagnetic Compatibility, 1981. **EMC-23**(4): p. 377-382.
49. Berenger, J.P., *Three-Dimensional Perfectly Matched Layer for the Absorption of Electromagnetic Waves.* Journal of Computational Physics, 1996. **127**: p. 363-379.
50. Weber-Bargioni, A., et al., *Functional plasmonic antenna scanning probes fabricated by induced-deposition mask lithography.* Nanotechnology, 2010. **21**(6): p. 065306.
51. Vučković, J., et al., *Optimization of the Q Factor in Photonic Crystal Microcavities.* IEEE Journal of Quantum Electronics, 2002. **38**: p. 850-856.
52. Tanabe, T., et al., *Single point defect photonic crystal nanocavity with ultrahigh quality factor achieved by using hexapole mode.* Applied Physics Letters, 2007. **91**(2): p. 021110.
53. Jin, R., et al., *Photoinduced conversion of silver nanospheres to nanoprisms.* Science, 2001. **294**(5548): p. 1901–1903.
54. Luk'yanchuk, B., et al., *The Fano resonance in plasmonic nanostructures and metamaterials.* Nature Materials, 2010. **9**: p. 707-715.
55. Hernandez, G., *Analytical description of a Fabry-Perot photoelectric spectrometer.* Applied Optics, 1966. **5**(11): p. 1745–1748.
56. Martínez, L.L., et al., *Kinetics of the dissolution of pure silver and silver-gold alloys in nitric acid solutions.* Metallurgical Transactions B, 1993. **24B**: p. 827–837.
57. Grass, M.E., et al., *Silver Ion Mediated Shape Control of Platinum Nanoparticles: Removal of Silver by Selective Etching Leads to Increased Catalytic Activity.* Journal of Physical Chemistry C, 2008. **112**: p. 4797-4804.
58. Chang, W.H., et al., *Efficient Single-Photon Sources Based on Low-Density Quantum Dots in Photonic-Crystal Nanocavities.* Physical Review Letters, 2006. **96**: p. 117401.

59. Barclay, P.E., et al., *Coherent interference effects in a nano-assembled diamond NV center cavity-QED system.* Optics Express, 2009. **17**(10): p. 8081–8097.
60. Mukherjee, I., G. Hajisalem, and R. Gordon, *One step Integration of metal nanoparticles in photonic crystal nanobeam cavity.* Optics Express, 2011. **19**(23): p. 22462–22469.
61. Johnson, S.G., et al., *Perturbation theory for Maxwell's equations with shifting material boundaries.* Physical Review E, 2002. **65**: p. 066611.
62. Parkash, A., J.K. Vaid, and A. Mansingh, *Measurement of dielectric parameters at microwave frequencies by cavity-perturbation technique.* IEEE Transactions on Microwave Theory and Techniques, 1979. **27**: p. 791–795.
63. Kumar, A., K. Thyagarajan, and A.K. Ghatak, *Analysis of rectangular-core dielectric waveguides: an accurate perturbation approach.* Optics Letters, 1983. **8**(1): p. 63–65.
64. Soljačić, M., et al., *Optimal bistable switching in nonlinear photonic crystals.* Physical Review E, 2002. **66**(5): p. 055601.
65. Waldron, R.A., *Theory of Electromagnetic Waves*. 1970, London: Van Nostrand Reinhold Co.
66. Haus, H.A., *Waves and Fields in Optoelectronics*. 1984, New Jersey: Prentice Hall Inc.
67. Johnson, P.B. and R.W. Christy, *Optical constants of the noble metals.* Physical Review B, 1972. **6**(12): p. 4370–4379.
68. HPC, C.C. *https://computecanada.ca*.
69. Mukherjee, I. and R. Gordon, *Analysis of hybrid plasmonic-photonic crystal structures using perturbation theory.* Optics Express, 2012. **20**(15): p. 16992-17000.
70. Yuan, C.T., et al., *Antibunching Single-Photon Emission and Blinking Suppression of CdSe/ZnS Quantum Dots.* ACS Nano, 2009. **3**(10): p. 3051-3056.
71. Yang, W., et al., *Spectroscopic characterization of streptavidin functionalized quantum dots.* Analytical Biochemistry, 2007. **364**: p. 193-203.
72. Yu, W.W., et al., *Water-soluble quantum dots for biomedical applications.* Biochemical and Biophysical Research Communications, 2006. **348**(3): p. 781-6.
73. Sherry, L.J., et al., *Localized Surface Plasmon Resonance Spectroscopy of Single Silver Nanocubes.* Nano Letters, 2005. **5**(10): p. 2034-2038.
74. Sönnichsen, C., et al., *Spectroscopy of single metallic nanoparticles using total internal reflection microscopy.* Applied Physics Letters, 2000. **77**(19): p. 2949.

Appendix A

Matlab code for Lorentzian fitting

```
function main

%% starting

fclose all;
close all;
clear all;
clc;
disp('# starting');
pause(0.1);

%% loading data from file

d=load('data.txt');
x=d(:,1);
yOrig1=d(:,2);
yOrig=yOrig1- min(yOrig1);
figure;
plot(x,yOrig,'ob','MarkerEdgeColor','k',...
             'MarkerFaceColor','k',...
             'MarkerSize',2 );
hold on;

%% define start point
y0=0;
A=40;
w=0.2;
x0=597;
vStart=[y0,A,w,x0];
fprintf('Start:  y0=%f  A=%f  w=%f  x0=%f\n',vStart(1),vStart(2),vStart(3),vStart(4));
yStart=fun(vStart,x);

%% using nlinfit

vEnd=nlinfit(x,yOrig,@fun,vStart);
yEnd=fun(vEnd,x);
fprintf('End:  y0=%f  A=%f  w=%f  x0=%f\n',vEnd(1),vEnd(2),vEnd(3),vEnd(4));
plot(x,yEnd,'-r', 'linewidth' ,1.5);

%% ending
disp('# ending');
```

```
xlabel('Wavelength (nm)');
ylabel('Intensity Counts');
figure;
[FitResults,MeanFitError]=peakfit([x' yOrig'],580,660,1,2);
```

###Called function “fun.m” applying Lorentzian formula###

```
function [y]=fun(v,x)
y0=v(1);
A=v(2);
w=v(3);
x0=v(4);
y=y0+(2*A/pi).*(w./(4*(x-x0).^2+w.^2));
```

Appendix B

Matlab code for applying Perturbation formula on simulation data

```
clear all;
clc;

mu0 = pi*4e-7;
eps0 = 8.854e-12;
c0= 1/sqrt(mu0*eps0);%speed of light in nm
eps_np=(0.05521+4.0111j)^2;  % Ag J & C refractive index at 600 nm
mu_np=1;
omega0=497.802e12;   % unperturbed cavity frequency
lambda0=602.232;
k=(2*pi*omega0)/c0; % wave vector
Q=54963.6;   % unperturbed cavity quality factor

%load data from the bare cavity simulations

Ef=load('nanobeamEx.txt');
Hf=load('nanobeamHz.txt');
E1=reshape(Ef,463761,1); %electric field V/nm
H1=reshape(Hf,463761,1); %magnetic field A/nm

%load normalized data from the nanoparticle simulations

E=load('rodEy_ynormal_in.txt');
H=load('rodHz_ynormal_in.txt');
Enp=reshape(E, 75651,1);
Hnp=reshape(H, 75651, 1);

 for tt=1:(length(Enp)-1)
    Epts= linspace(Enp(tt), Enp(tt+1), 7);

    for tp=1:7
    Enew(tp,tt)=Epts(tp);

    end
 end
  Enew(1,:)=[];
 Ep=reshape(Enew, 453900,1);
 Eprime=vertcat(Enp(1), Ep);

 for tt=1:(length(Hnp)-1)
    Hpts= linspace(Hnp(tt), Hnp(tt+1), 7);
```

```
    for tp=1:7
    Hnew(tp,tt)=Hpts(tp);

    end
 end
Hnew(1,:)=[];
Hp=reshape(Hnew,453900,1);
Hprime=vertcat(Hnp(1), Hp);

 ind1=1:4930;
 ind2=440000:444929;
 E1(ind1)=[];
 H1(ind1)=[];
 E1(ind2)=[];
 H1(ind2)=[];

E2=Eprime-E1;
H2=Hprime-H1;
Dprime=eps_np*eps0.*Eprime;
Bprime=mu_np*mu0*Hprime;
D1=eps0.*E1;
D2=Dprime-D1;
B1=mu0.*H1;
B2=Bprime-B1;

var4=(H2.*B1)-(H1.*B2);
var5=(H1div.*E2div)+(E1div.*H2div);
var1=(((E2.*D1)-(E1.*D2))-var4);
var2=((E1.*D2)-(H1.*B2));
var3=((E1.*D1)-(H1.*B1)+var2);

V1=6800e-9*6800e-9*1800e-9; %volume of the cavity
S1=2*(6800e-9*6800e-9+ 6800e-9*1800e-9+ 6800e-9*1800e-9); %Surface area of the
cavity
V2=150e-9*150e-9*500e-9; %volume of the near field region assumed around the cavity
dv1=0:V1/453900:V1;
ds1=0:S1/75650:S1;
dv2=0:V2/453900:V2;
int1=trapz(dv1,var3);
int3=trapz(ds1, var5)/(1j*omega0);
int2=(trapz(dv2,var1));
int4=int2-int3;
delfreq=real((int4./int1))*omega0

d=-imag((int4./int1));
```

```
 % ad-hoc calculation of scattering losses
load('3026_5_si3n4_tfsf.mat');
Cabs=sigmaabs(39); % absorption cross Section in m^2
Cscat=sigmascat(39);%scattering cross Section in m^2

% Calculation of quality factor
Qabs=1./(2.*(d + (1/(2*Q))))
tau_abs=Qabs./(omega0+delfreq)
tau_scat=tau_abs.*(Cabs./Cscat)
Qscat=(omega0+delfreq).*tau_scat
beta_r=(1./tau_abs)+(1./tau_scat);
tau_r=1./beta_r
Qr=tau_r.*(omega0+delfreq)
```